Fractionation of Particle Suspensions in a Viscoplastic Fluid: Towards a Novel Process

by

Ario Madani

B.Sc., Shiraz University, 2005

A THESIS SUBMITTED IN PARTIAL FULFILLMENT
OF THE REQUIREMENTS FOR THE DEGREE OF

Doctor of Philosophy

in

THE FACULTY OF GRADUATE STUDIES
(Mechanical Engineering)

The University Of British Columbia
(Vancouver)

July 2011

Abstract

The focus of this thesis is the separation or sorting of particle suspensions in a yield stress or viscoplastic fluid. Although the process is applicable to most industrial suspensions, the motivation of the work stems from pulp and paper industry, i.e. papermaking and microfibrillated cellulose (MFC) suspensions. The work is presented in four different yet complementary studies.

In the first study, the concept of particle fractionation in a viscoplastic fluid is introduced. Here this novel principle is demonstrated, batch wise, by measuring the difference in centrifugal force required to initiate motion of an initially stable particle suspension in a gel. The criteria for motion is delineated as the ratio of the centrifugal force to yield stress as a function of particle size and orientation. Demonstration experiments are given to illustrate that the separation process is very efficient.

In the second and third studies we demonstrate the principle on two industrial suspensions, i.e. a SBK (semi-bleached kraft) papermaking fibre and MFC. With papermaking fibres, it is shown that efficient separation, based upon cell wall thickness can be achieved. With MFC, it is shown that the process is more efficient

than traditional separation techniques, i.e hydrocyclone and pressure screen.

In the final study, we speculate regarding the conditions required to make a continuous process based upon the batch testings. Here, it is identified that a spiral Poiseuille flow would be sufficient to achieve separation. The questions addressed in this study are what is the size of the unyielded region for this flow field and what is the bound for transition to turbulent flow. It was found that the magnitude of the swirling flow does not affect the size of the plug and the axial velocity is decoupled from the rotational rate. In addition, the yielded region is always formed in the middle of the annular gap. To address the flow state, a linear stability analysis was performed using the method of normal modes. The flow was found to be linearly stable for all conditions tested.

Preface

Four chapters of the thesis have been submitted or will be submitted for publication in refereed journals as following:

1. Chapter two: **Madani A.**, Storey S., Olson J.A., Frigaard I.A., Salmela J. and Martinez D.M. 2010 "Fractionation of non-Brownian rod-like particle suspensions in a viscoplastic fluid" Chem. Eng Sci 65(5), 1762-1772.

   This research was initiated by J. Salmela and S. Storey and Figures 2.2 and 2.12 are unpublished results of their initial work. Dr. Friggard has been helpful with his ideas throughout the research and my research has been co-supervised by Dr. Martinez and Dr. Olson. I planned, designed and performed all the experiments and wrote the article.

2. Chapter three: **Madani A.**, Olson J.A., Martinez D.M., and Fung, A. (2010). "Novel methods to characterize and fractionate papermaking fibres" Nordic Pulp and Paper Res Journal, Vol. 25, Issue 4, pp. 448-455.

   A. Fung worked as a Co-op student under my supervision and had contributions in this research. Dr. Martinez and Dr. Olson supervised the research

and I planned, designed and performed all the experiments and wrote the article.

3. Chapter four: **Madani A.**, Kiiskinen, H., Olson J.A., and Martinez D.M., (Accepted). "Fractionation of microfibrillated cellulose and its effects on tensile and elongation of paper" Nordic Pulp and Paper Res. Journal, Vol. 26, Issue 3.

   H. Kiiskinen provided us with the material and supervised this part of research when it was performed in VVT, Finland. I planned, designed and performed all the experiments and wrote the article.

4. Chapter five: **Madani A.**, Olson J.A., Frigaard I.A., and Martinez D.M., (to be submitted). Stability analysis of spiral Poiseuille flow of Newtonian and Bingham fluids.

   I performed the stability analysis and wrote the paper under the supervision of Dr. Martinez, Dr. Frigaard and Dr. Olson.

Table of Contents

List of Tables

List of Figures

Nomenclature

Symbols

a_0	constant	m^{-1}
a_1	constant	
A_e	area of the envelope around the particle	m^2
B	Bingham Number	
C	coarseness	mg/m
d_c	diameter of the cylindrical particle	m
D	diameter	m
$\hat{d}$	characteristic length	m
F	applied force	N
$\mathbf{g}$	gravity	m^2/s
G	pressure gradient	Pa/m

H	channel width	m
L	length of the cylindrical particles	m
ℓ	inverse of specific surface	kg/m^2
M	total mass of the fibres	kg
m	mass fraction of each class of fibres	
N	total number of the fibres	
p_{ij}	probability	
$\mathbf{p}$	orientation	
p	fluid pressure	Pa
r	aspect ratio	
R	radius	m
Re	Reynolds number	
$\mathbf{u}$	velocity vector	m/s
u'	radial perturbed velocity	m/s
U	radial velocity	
$\hat{U}_0$	characteristic velocity	m/s
V	volume	m^3

$\hat{V}$	tangential velocity	m/s
v'	tangential perturbed velocity	m/s
W	axial velocity	
w'	axial perturbed velocity	m/s
$\mathbf{x}$	vector	

Subscripts

c	critical
i	initial
i	imaginary part of a complex function
p	particle
t	time derivative
z	axial
r	radial
r	real part of a complex function
θ	tangential

Greek Letters

α	wave number

μ	dynamic viscosity of the fluid	$Pa.s$
η	radius ratio	
$\dot{\gamma}$	shear rate	s^{-1}
θ	tangential direction	
τ_y	yield stress	kg/m^2
τ	deviatoric stress tensor	kg/m^2
ρ	density of the fluid	kg/m^3
ω	rotational velocity	
ϕ	volume fraction	kg/m^3
ε	perturbation parameter	
λ	temporal wave number, eigenvalue	

Acknowledgments

Many individuals have contributed to this research and their assistance is gratefully acknowledged. I sincerely thank the following individuals for their help throughout the course of this project:

My co-supervisors; Dr. Mark Martinez and Dr. James Olson for their guidance, suggestions and valuable discussions throughout the course of this research. Without their insight both into my research and personal development, I don't believe I could have ever achieved all that I have.

In addition I would like to thank Harri Kiiskinen at VTT, Finland who provided us with MFC and experimental instruments and George Soong who was always very helpful with all the technical issues.

We gratefully acknowledge financial support of the Natural Sciences and Engineering Research Council of Canada through the Collaborative Research and Development program and through the support of our partners BC Hydro, FPInnovation, Catalyst Papers, Howe Sound Pulp and Paper, West Fraser Quesnel River Pulp, Canfor, Andritz, Arkema, Honeywell, WestCan Engineering, Advanced Fiber Technologies, Ontario Power Authority and CEATI international.

Last but not least, my parents and my sisters for their love, encouragement and support in realizing this dream.

Dedication

To my family for their love and support;

my friends, and Professors

بِسْمِ اللَّـهِ الرَّحْمَـٰنِ الرَّحِيمِ

الْحَمْدُ لِلَّـهِ الَّذِي هَدَانَا لِهَـٰذَا وَمَا كُنَّا لِنَهْتَدِيَ لَوْلَا أَنْ هَدَانَا اللَّـهُ

(۴۳ اعراف)

ســپاس خدای را که ما را بــه اینجــا رهنمون شـد، اگـر خداونـد راهـبر نمـی شـد هـرگز راه نمـی یـــــافتیم

Chapter 1

Introduction

The focus of the present work is the study of separation or fractionation of different classes of non-Brownian particles in a yield stress fluid. The motivation for the present work stems from an interest in one particular particle suspension, i.e. papermaking fibre suspensions. Papermakers fractionate to allow targeted processing of the low quality fraction to improve product performance while minimizing the amount of processing and subsequent energy, chemicals and capital required. The pulp fractions can also be used to produce papers with radically different properties. For example, fractionating the short fibre fraction from the long fibre fraction can create a short fibred paper that has excellent printing characteristics and a long fibred paper with high tensile strength. Further, the fibre fractions can be blended to create a spectrum of products designed for each of the many paper applications.

There are essentially two industrial methods to fractionate pulp fibres in use

today: pressure screens and hydrocyclones. In pressure screen, the fibre suspension is fed into the annular gap between a rotor and an outer cylinder containing small apertures. The screen apertures are either narrow slots (as small as 0.1mm wide) or small diameter holes (as small as 0.8mm in diameter). The surface of the cylinder can either be smooth or be contoured. Separation here is based upon length as the small particles pass through the apertures. Several studies have been completed to understand how the operation and design of screens and screening systems affect fibre fractionation efficiency and general reviews of the topic are given by Sloane (2000) and Julien Saint Amand and Perrin (1999).

With regards to the hydrocyclone, there are a number of experimental studies that have shown that these devices are able to separate fibres based on its specific surface (fibre surface area per gram). This results in a separation of earlywood, large diameter thin walled fibres from latewood, small diameter, thick walled fibres, e.g, Paavilainen (1992). In addition, hardwood vessel elements have been shown to be effectively removed by hydrocylones.

The efficiency for fractionation in both hydrocyclones and pressure screens is known to be relatively low. The inherent separation potential is not realized because of the complexity of the flow within theses devices. A stochastic element is introduced into the system through turbulence, the presence of boundaries, flocculation, and long range hydrodynamic interactions; these effects diminish the efficiency of the separation process. In this work a new principle for fractionation is proposed and a series of experiments demonstrating its utility is presented. Here we show that fractionation can indeed proceed based on either length, diameter or

density.

This thesis is presented in 6 chapters. In chapter 1 the motivation for the work is given. Chapter 2 introduces both the novel concept as well as a thorough discussion of why the currently available methodologies are inefficient. The utility of the novel principle is demonstrated through separation of a number of ideal particles. In chapter 3 and 4 the methodology is extended to two industrial suspensions, namely an SBK (semi-bleached kraft) pulp and an MFC (Microfibrillated Cellulose) suspension. In chapter 5, an introduction is given regarding the flow field required to achieve separation using this principle in a continuous device. The highlights of the work are summarized in chapter 6.

Chapter 2

The Novel Fractionation Technique

2.1 Introduction

[1] In this chapter we propose a new principle for fractionation and present a series of experiments demonstrating its utility. In §2.1.1, the literature review, we present the background material leading up to this novel principle. Here we demonstrate first why separation with a Newtonian fluid is inefficient and then proceed to develop and justify the novel principle. In §2.2-2.3, simple experiments highlighting this principle are described and the results are discussed. The foreseeable limitations of this process are discussed in §2.4.

[1] Parts of this chapter is published in: **Madani A.**, Storey S., Olson J.A., Frigaard I.A., Salmela J. and Martinez D.M. 2010 "Fractionation of non- Brownian rod-like particle suspensions in a viscoplastic fluid" Chem. Eng Sci 65(5), 1762-1772.

2.1.1 The Underlying Fractionation Mechanism

Understanding the relative motion of particles in a flowing fibre suspension undergoing fractionation is difficult. Insight into this mechanism can by gained by first examining the simplest case of the motion of an isolated particle settling in an unbounded fluid, under the influence of gravity. An important case occurs when the particle is traveling at its steady terminal velocity u where the net weight of the particle is exactly counterbalanced by the drag force F_d, i.e.[2]

$$F_d = \Delta\rho V g \tag{2.1}$$

where V is the volume of the particle; $\Delta\rho = (\rho_p - \rho)$ is the difference in density between the particle ρ_p and the fluid ρ, and g is the acceleration due to gravity. If the drag coefficient C_d is defined as

$$C_d = \frac{2F_d}{\rho u^2 A} = \frac{2\Delta\rho V g}{\rho u^2 A} \tag{2.2}$$

and the inverse of specific surface of the particle is assigned to be $\ell = V\rho_p/A$, Equation 2.2 can be rearranged to give

$$u^2 C_d = 2\ell g(\frac{\Delta\rho}{\rho\rho_p}) \tag{2.3}$$

[2]In this simple example we assume that the particle does not rotate nor drift from the gravity direction. We do so for clarity in the presentation and this assumption does not distract from the main point of this simple example

This indicates that the terminal velocity is proportional to the specific surface of the particle and strongly supports the fractionation mechanism advanced by Paavilainen (1992).

The equation derived above applies for all classes of particles. We can gain further insight into the fractionation process by examining one class of particles in which a closed form analytical expression can be derived for the drag coefficient. This is the case of cylindrical particles settling under creeping flow conditions, that is where $Re \to 0$, where Re is the Reynolds number based upon the length of the fibre. This work was performed originally by Batchelor (1972), and subsequently extended by Mackaplow and Shaqfeh (1998), and indicates that the terminal velocity is given by a function of the form

$$\mathbf{u} = \frac{\Delta\rho d_f^2}{16\mu}[(\ln 2r + 0.193 + O(\ln 2r)^{-1})\mathbf{g} + (\ln 2r - 1.807 + O(\ln 2r)^{-1})(\mathbf{p}\cdot\mathbf{g})\mathbf{p}] \tag{2.4}$$

where r is the aspect ratio of the fibre defined by L/D; μ is the viscosity of the fluid; and $\mathbf{p}$ is a unit vector that indicates fibre orientation. The **bold** font indicates a vector quantity. This equation implies that unlike spheres, fibres can have significant motion perpendicular to gravity; the drift velocity is strongly dependent upon its orientation. Jayaweera and Mason (1965) indicate that with $Re < 0.01$, cylinders do not tend to rotate during settling - they tended to fall in the same attitude with which they were released. The key finding here is that for cylindrical particles, the terminal velocity is not a unique value based upon the properties of the particles. With these findings, one can argue that a mechanis-

tic means of separating particles exists. Under more realistic conditions, i.e. at elevated concentrations and Reynolds numbers, disturbances must be introduced into the suspension which would result in a distribution in the terminal velocity. We shall consider two classes of disturbances below and characterize the resulting distributions in the terminal velocity.

In the first case, category 1, we consider disturbances in the suspension created by the presence of other particles. The concentration of the fibre suspension need not to be large and we restrict our argument to the influence of the "wake" of one particle moving in the vicinity of another. This phenomenon is not new. With swarms of settling particles Happel and Brenner (1965) explain that the physics becomes more complex as each individual fibre settles and rotates under the influence of the "wakes" or "long-range hydrodynamic disturbances" of the other settling particles . This leads to inhomogeneous settling rates and local floc formation. With monodisperse glass fibre suspensions, floc formation has been observed by Kumar and Ramarao (1991) who noted that as the fibre concentration increased, the number of flocs increased and caused greater hindrance effects. To help understand this behavior, Herzhaft and Guazzelli (1999) visualized the motion of marked glass fibres, in a suspension of unmarked fibres made optically transparent by matching the index-of-refraction. By doing so, they were able to measure both the velocity and orientation of a particle. They found that in the dilute regime, the ensemble-averaged settling velocity *actually increases* with concentration and *may exceed* the velocity of an isolated particle. They also observed that under these conditions most of the fibres were aligned in the di-

rection of gravity. In the semi-dilute regime, however, the sedimentation velocity decreased according to the Richardson-Zaki correlation (Richardson and Zaki , 1954). There are only a few numerical simulations available in the literature which attempt to describe this process under these conditions (Koch and Shaqfeh , 1998; Mackaplow and Shaqfeh , 1998; Butler and Shaqfeh , 2002). In general these works were conducted in the limit of $Re \to 0$, using slender body theory, and suggest that the settling suspension should segregate into particle clumps. Koch and Shaqfeh (1998) were the first to describe an instability mechanism that leads to floc formation. They advanced an argument that a 'test' fiber in the velocity field far from a sedimenting single fiber tends to orient its main axis such that the relative velocity of the two particles became negative. Thus, the particles will tend to form clusters until near-field effects or contact forces intervene. Mackaplow and Shaqfeh (1998) present two results using (i) Monte-Carlo simulations of static fibre assemblies and (ii) point-particle approximations for the dynamic case. They observed fibre clustering and velocities greater than that of an isolated particle. Steady state, however, was not reached by the end of the simulations. Butler and Shaqfeh (2002) simulated the motion of swarms of particles in the limit of zero Reynolds numbers using slender-body theory. They observed fibre clustering and a fibre rich stream in the middle of the computational domain. Their simulations were in good agreement with experimental results of Herzhaft and Guazzelli (1999).

We continue this discussion by considering the second category of disturbances which are created at elevated Reynolds numbers. Our attention is focused

on this regime as this *Re* range represents the range relevant for papermaking fibres settling in water (Marton and Robie , 1969). It has been shown that, unlike in the Stokes' regime, at Reynolds numbers $Re \sim O(1)$ isolated non-spherical particles tend to exhibit preferential orientation during settling(Jayaweera and Mason , 1965; Feng et al. , 1994; Jianzhong et al. , 2003). The torque induced on thin cylinders causes the body to rotate into a stable position with its symmetry axis aligned horizontally. Feng et al. (1994) show that particles migrate towards the center of the channel due to wall effects. At elevated concentrations, the long range hydrodynamic interactions perturb the flow field to the point where recirculation or swirling like structures are apparent (Holm et al. , 2004). A representative case displaying this phenomenon is given in Figure 2.1.

The result was visualized using particle image velocimetry, a common flow visualization method, and is reported at four different times. The initial concentration of the suspension in this case was 0.3 % (vol/vol); this is equivalent to a crowding number[3] of $N = 5$ which represents roughly handsheet concentrations. What is clear in Figure 2.1 is that the particles recirculate while settling. Clearly, this indicates that the terminal velocity is not a unique value as this stochastic swirl is superimposed on the settling motion. In later work Salmela et al. (2007) completed a more comprehensive study using a similar index-of refraction matching technique and studied the motion of settling particles as a function of concentration, aspect ratio, fluid viscosity, and fibre length for both monodisperse and

[3]The crowding number N describing the number of fibres of length L and diameter D within a certain volume element at a given volume concentration (Kerekes et al. (1985))

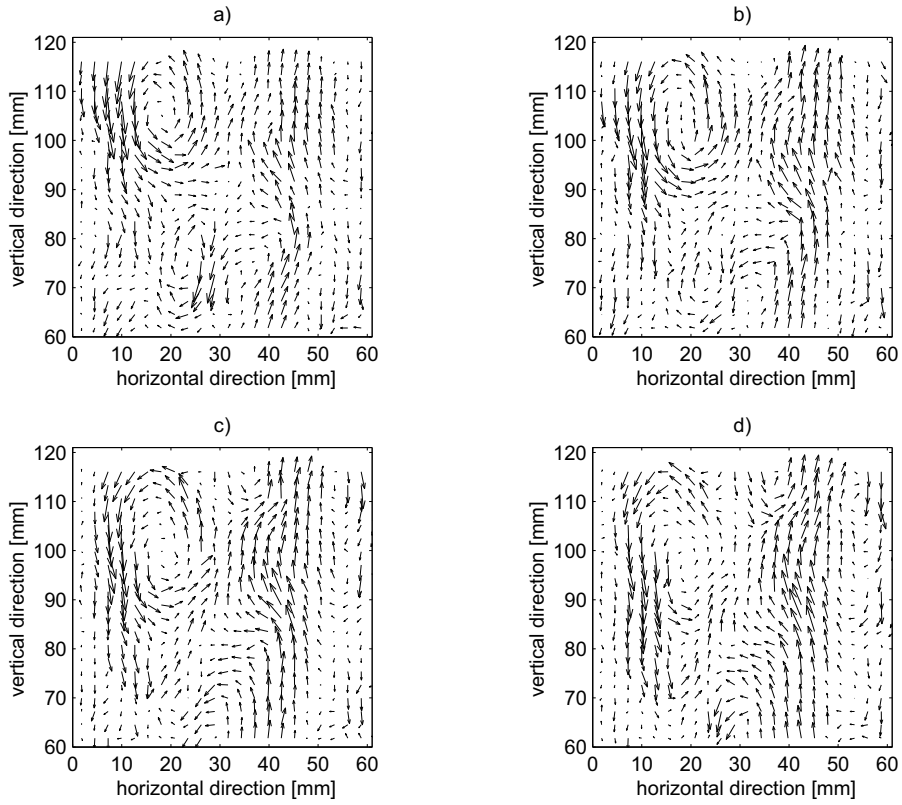

Figure 2.1: The motion of index of refraction matched 5mm in length glass fibre suspension settling in a viscous fluid (Holm et al. , 2004).

bidisperse suspensions. What sets this work apart is that the motion of tracer fibres could be tracked three-dimensionally; hence fibre fractionation could be studied in this equipment. Like Herzhaft and Guazzelli (1999), Salmela et al. (2007) reported non-monotonic behaviour in the average settling velocity as a function of concentration with the maximum velocity occurring at a volume fraction of $\phi = 0.05\%$. With papermaking fibres, non-monotonic behaviour has also been

observed with the maximum in the initial settling speed occuring at a crowding number of $N \sim 16$ (Holm et al. , 2004). Salmela et al. (2007) also indicated that the orientation state of the suspension also displayed complex behaviour under these conditions. They report that the suspension was preferentially oriented in the horizontal state at low concentrations and then adopted an increasing proportion of fibres in the vertical state as concentration increased.

We now turn to what we consider the key findings from unpublished results of Salmela and his coworkers which sheds light onto the mechanistic understanding of the ability to fractionate based upon settling. Although not reported in Salmela et al. (2007), the results stem from this study. Here they examine the motion of a bidispersed suspension comprised of glass rods of two different aspect ratios $r = 23$ and 50 and measured the ensemble-averaged settling velocity of each class of particle. These authors measured this velocity as a function of the initial suspension concentration, see Figure 2.2. Here the results have been made dimensionless by scaling with the average of the isolated velocity of the two different particles settling in the vertical position; these values were determined by experiment. What is clear from this figure is that under dilute conditions each fibre fraction settles at statistically different velocities. In this region fractionation may be possible. With increasing concentration, the differences between the terminal velocities diminish until their difference is indistinguishable. To summarize the existing literature, we find that for isolated particles in an unbounded fluid the terminal velocity is related to the density, diameter, aspect ratio and orientation of the cylinder. Under creeping flow conditions with extremely dilute suspensions,

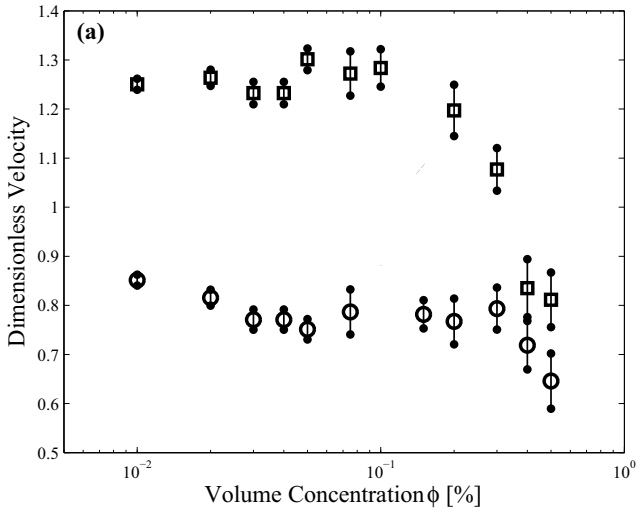

Figure 2.2: Dimensionless mean settling velocity versus volume concentration ϕ for a bidispersed suspension comprised of equal masses of particles with aspect ratios of $r = 50\%$ (□) and $r = 23\%$ (○). The uncertainty in the estimate is reported as the 95% confidence interval. The Reynolds number in this case based upon the average fibre length was estimated to be $Re = 0.12$.

we can draw the conclusion that we can indeed separate fibres based upon the terminal velocity, if and only if, the orientation distribution remains constant during descent. We find that at elevated concentrations, for all *Re* above the creeping flow conditions, long range hydrodynamic disturbances lead to floc formation and swirling chaotic structures. Salmela et al. (2007) have shown that there is no statistical difference between the terminal velocity at any reasonable concentration. Hence efficient separation would be impossible. As a result, this present study is motivated from these findings and our goal is to develop an efficient method.

2.1.2 Hydrodynamics of a Hydrocyclone

With this understanding of how particle suspensions move in simple flow field, we attempt to describe the flow field that occurs in a hydrocyclone. Clearly the flow field in the hydrocyclone is three dimensional, i.e. there are three components of flow which vary both in the radial and axial directions. At long-time scales the flow is considered axi-symmetric, i.e. the order of magnitude of the radial and axial flows must be similar; the swirl or tangential flow is the dominant flow component in this device. The salient point here is that the flow is quite complicated in the inlet region and with certain devices flow reversal occurs in the central core of the hydrocyclone. Further details of this flow field are given by Ko (2005), Narashima et al. (2007), and Nowakowski and Dyakowski, (2003) and the references contained therein.

Perhaps the most relevant work in the this area is that by Bergström and Vomhoff (2007). Here they map out the flow field in cylindrically shaped hydrocyclone using both a pitot tube to measure the tangential component and ultrasound velocimetry to measure the radial component. With regards to the tangential body, these authors report that under dilute conditions the flow field observed resembles quite closely to a combination of free and forced vorticies. At higher conditions, namely after 7.5 g/L mechanical entanglement dominates and creates a flow field which resembles solid body rotation.

A number of research groups, Hsieh and Rajamani (1991) and Sevilla and Branion (1997), have attempted to predict particle trajectories in these devices under extremely dilute conditions. These models are generally considered to be

coupled “one-way”, i.e. the fluid affects the particle motion and not the other way around. Expressions for radial movement of particle was obtained by balancing the centrifugal force with the radial component of the drag force; this form of balance equation is very similar to that considered for the settling isolated particle described in the previous section. Similarly, for particle motion in axial direction, these authors equate the gravity force with the axial drag force. Boysan et al. (1982) and Ma et al. (2000) determined the particle drag force and used it in a stochastic particle tracking technique. In their method, they did not consider the velocity fluctuation due to turbulence while formulating the drag force equation. A discrepancy was noticed between the behaviors of small particles when compared to experimental results.

What is clear in this body of literature is that the tangential flow creates a centrifugal force which causes particle migration in the radial direction. For the residence time of the fibre in this device, the separation efficiency is largely dependent upon the ability of the particle to migrate in the radial direction. In the previous section, we advanced the argument that the terminal velocity of an isolated particle is not the sole indicator of the ability to migrate. The mobility of the fibre is also a function of long range hydrodynamic disturbances and flocculation. The flow field in the hydrocyclone is turbulent and this too will hinder particle migration and diminish the separation efficiency.

2.1.3 Towards a Novel Fractionation Principle

From the above review we see that the motion of a particle suspension at any industrially relevant concentration and Reynolds numbers is extremely complex. Chaotic behavior is evident due to long-range hydrodynamic interactions. Since these observations were made under ideal settling conditions, we anticipate an even richer behavior to occur in the complex three-dimensional, turbulent flow fields encountered in industrial hydrocyclones (Ko (2005); Narashima et al. (2007); Nowakowski and Dyakowski, (2003); Bergström and Vomhoff (2007); Hsieh and Rajamani (1991); Sevilla and Branion (1997); Boysan et al. (1982); Ma et al. (2000)). As a result, instead of trying to improve an already complex coupled fluid-fibre interaction problem, we attempt to devise a new separation principle which is not hindered by long-range disturbances. We feel that this may be achieved through use of a yield stress fluid [4].

To introduce our novel fractionation principle we consider once again the illustrative problem of an isolated particle settling in a yield stress fluid. With yield stress fluids, the settling problem is more complex: the presence of a yield stress implies that settling can only occur if the net applied force F_a is greater than the resistive force due to the yield stress of the material. Despite the simplicity of the problem, the mechanism by which the particle settles is poorly understood. Clearly a critical force is required to initiate the motion of the particle. To highlight this, consider as an example a particle immersed in a material having a yield

[4] Everyday examples of yield stress fluids are ketchup, mayonnaise, and salad dressing. With these fluids, the yield stress is the applied stress that must be exceeded in order to make the fluid flow. Ketchup has a yield stress of approximately 15 Pa.

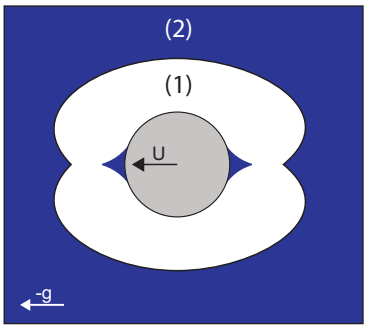

Figure 2.3: Schematic illustrating the yielded (region (1)-white) and unyielded flow regions (region (2)-blue), according to the numerical results by Beris et al. (1985). This figure was reproduced from Putz et al. (2008).

stress τ_y. If F_a is not sufficient to overcome the resisting force then the object will be suspended indefinitely. Motion will commence when

$$F_a > \tau_y A_e \tag{2.5}$$

where A_e is the surface area over which the force due to the yield stress is applied. The exact value for A_e however remains an open question. The above relationship can be made dimensionless by scaling each side by a characteristic area of the particle. In this case if we divide each side of the equation by D^2, we can define a dimensionless force ratio F which represents the criteria for motion

$$F = \frac{F_a}{\tau_y D^2} > \frac{A_e}{D^2} \tag{2.6}$$

The bound where motion begins is defined as the critical force ratio F_c.

The key to the separation is the determination of A_e. A number of researchers

have attempted to determine A_e through simulation and we divide the methods into four groups. In the first category are estimates made through an assumption regarding the shape of A_e. For example, through a simple force balance Andres (1961) argues that for spherical particles A_e is related to the projected area of the particles and reports that motion should commence when $F_c = 4.8$. In the second category are regularization models in which a continuous function is used to approximate the rheological behavior of the yield stress fluid (Blackery and Mitsoulis , 1997; Liu et al. , 2002; Beaulne and Mitsoulis , 1997; Jie and Zhu , 2006). In essence this approach avoids the singularity inherent with strain rate decreasing to zero in unyielded regions. A detailed review of this is given in Frigaard and Nouar (2005). These authors advance the argument that these regularization methods converge to the correct flow field, but cannot recover the effective area properly. The third category of methods involves domain mapping. In this category falls the work of Beris et al. (1985), which we consider to be the benchmark paper in this area. Combining a regularized model with an intricate mapping of the yield surfaces onto a standard domain, they were able to calculate the position of the yield surface of a settling sphere very accurately for one class of yield stress fluids, that is a Bingham plastic [5]. By doing so they argue that two yield surfaces are evident: a kidney shaped surface in the far field and two somewhat triangular-cusps attached to the leading and trailing edges of sphere (Figure 2.3). With this,

[5] A Bingham plastic is a viscoplastic material that behaves as a rigid body at low stresses but flows as a viscous fluid at high stress. When flowing, there is a linear relationship between the applied stress and the strain rate.

these authors indicate that particle motion would commence when

$$F_c = \frac{V\Delta\rho g}{\tau_y D^2} \approx \frac{7\pi}{2} \approx 11 \tag{2.7}$$

This expression is approximately 3 times greater than that given by Andres (1961) and are closer in magnitude to the experimental measurements of Tabuteau et al. (2007), Attapatu et al. (1995), Jossic and Magnin (2001), and Laxton and Berg (2005), i.e. $16 < F_c < 25$. In the fourth category are simulations conducted using augmented Lagrangian schemes (Glowiniski and Le Tallek (1987), Fortin and Glowiniski (1983)). Roquet and Saramito (2003) combined the augmented Lagrangian method with anisotropic grid refinement to obtain very accurate numerical results and have applied this method successfully to the flow around settling cylinders.

We now turn our attention to the experimental literature. An extensive summary of settling and sedimentation experiments in different media, including viscoplastic fluids, can be found in the book by Chhabra (2007). This review was published in 2007 and focuses generally on the calculation of the drag coefficient and the terminal velocity, i.e. engineering properties useful for design purposes. Recently there has been renewed interest in this problem due to the availability of (digital) particle image analysis (PIV). Gueslin et al. (2006), for example, used this technique to measure the flow field of a spherical particle settling in Laponite, an extremely thixotropic yield stress fluid. The objective of this work was to study the aging properties of this fluid. Putz et al. (2008) experimentally estimated A_e

through flow visualization experiments for two different size spheres settling in Carbopol solutions. Their results indicate that the shape of the yield surface approximates that of an ovoid spheroid with its major axis approximately 5 times greater than the radius of the particle.

To summarize, what is clear from this body of work is that during settling the flow is confined in the vicinity of the particle within an envelope the size of which is related to the yield stress of the material. For particles to settle, a critical force must be applied to overcome the resistance created by the yield stress. Relatively little is known about the shape of this surface and the magnitude of the applied force to create motion. What can be said is that the unyielded envelope is larger than the body itself but its shape has yet to be determined rigorously.

What is key in this description is that the differences in static stability of particles in a yield stress fluid, under the influence of an applied force, may represent a novel criterion for separation. We expand upon this idea to highlight the principle. In this study, we consider two different particles of equal dimensions but of different densities. Each particle is spun in a centrifuge at exactly the same angular velocity and at equal radial positions from the axis of rotation. In other words they experience the same acceleration field. The particle with greater density, however, experiences a larger centrifugal force as it has a larger mass. If we apply Equation 2.5, we see that separation of these two particles will occur if $F_{a_1} > \tau_y A_e > F_{a_2}$, where F_{a_1} and F_{a_2} are the centrifugal forces applied to each particle. This simple example leads us to the question: can we choose an applied force and a yield stress in which separation of particles is achieved? In this work we attempt to address

this question and devise simple experiments to illustrate this principle.

2.2 Experimental Details

In this work we measure the critical force required to initiate motion of a particle in a yield stress fluid under the action of a centrifugal force. Two different centrifuges were used depending upon the force required. For low rotational speed experiments an in-house centrifuge was built. In this case, the centrifuge, which was made from Plexiglas, was 250 cm in diameter, and 5 cm thick and was driven by a motor and controller, with a precision of 5 rpm, up to a maximum of rotational rate of 300 rpm. High speed experiments were conducted in a Universal Model UV centrifuge at rotational rates of up to 3000 rpm.

The main fluid used in this study was Carbopol-940 obtained from Noveon. In most of the work a 0.16% (wt/wt) solution was prepared using DI water and then neutralized using a dilute *NaOH* solution. The density of the resulting solution was that of water. The resulting gels were degassed and then allowed to rest overnight. Rheological characterizations were performed at room temperature in a cone and plate flow geometry on a Bohlin rheometer. Shear sweeps were performed in controlled strain mode typically in the range of $1 \times 10^{-2}\,\mathrm{s}^{-1}$ to $1\,\mathrm{s}^{-1}$ in order to determine the yield stress, a typical rheogram is shown in Figure 2.4(a) and the yield stress was estimated at the maximum of the curve shown in Figure 2.4(b). Here the uncertainty in the estimate is large. This is typical of most reported estimates for this parameter.

A number of different studies were performed in which density, diameter, as-

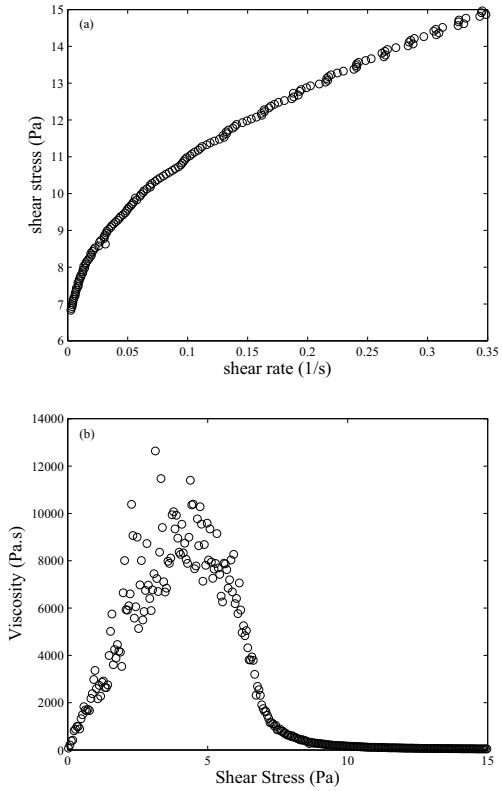

Figure 2.4: (a) A typical rheogram of shear stress versus shear rate for a 0.16% Carbopol solution. The local viscosity versus the shear stress for the same solution is given in (b). The yield stress is given at the maximum in this curve.

pect ratio, shape (degree of curl) of cylindrical rods were employed. Both rigid and flexible rods were considered.The particles were made from aluminum, brass and stainless steel and were manufactured by McMaster Carr. In our initial study, spherical particles were under the conditions outlined in Table A.1. Here particles were placed in the low speed centrifuge at a radial distance R from the axis of rotation and then spun at a fixed angular velocity ω for approximately 5 minutes.

At the end of the experiment, the position of the sphere was inspected and if unchanged (to within a prescribed tolerance), the test was repeated by increasing the speed of the centrifuge. The procedure continued until motion was induced. With this the critical force ratio to induce motion was estimated using the following expression

$$F_c = \frac{\Delta\rho V R\omega^2}{\tau_y D^2} \tag{2.8}$$

It should be noted that the Carbopol solution was pretreated before data collection by allowing a number of spheres to settle in the solution. Both Attapatu et al. (1995) and Putz et al. (2008) indicate that reproducible settling experiments can be obtained if approximately 4-5 spheres are allowed to settle in the gel.

In the second series of experiments we examined the stability of cylinders. In Tables A.2 - A.5 a large series of experiments were conducted to measure F_c as a function of the density and aspect ratio L/D of the rod, the angle of orientation (relative to the direction of motion), and its shape, that is the degree of kink reported as S/L. S/L is defined as the end-to-end length S divided by the length of the rod. In these studies, the orientation is defined by the direction of the chord connecting the two ends of the rod relative to the direction that the force is being applied. For the bent fibres as this is difficult to visualize so a schematic of this is shown in Figure 2.5.

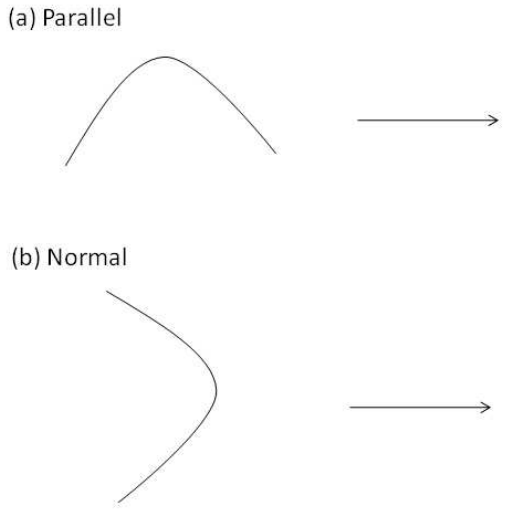

Figure 2.5: Schematic illustration of the orientation of bent rods used in the device. We define "parallel" to indicate the direction of the chord between the ends of the fibre make in relation to the direction of motion. In (a), we see that this is parallel to the direction of motion. In (b), the orientation is perpendicular to the direction of the applied force.

2.3 Results and Discussion

2.3.1 Spheres

Before proceeding to present the main findings of this section, it is instructive to examine the histograms of one test. As shown in Tables A.1 - A.5, a large number of tests were conducted for each experimental condition from which we could develop both a histogram and a cumulative probability distribution. An example of this is shown in Figure 2.6 where the histogram is smooth and clustered around a definite value. The cumulative distribution represents the fraction of particles

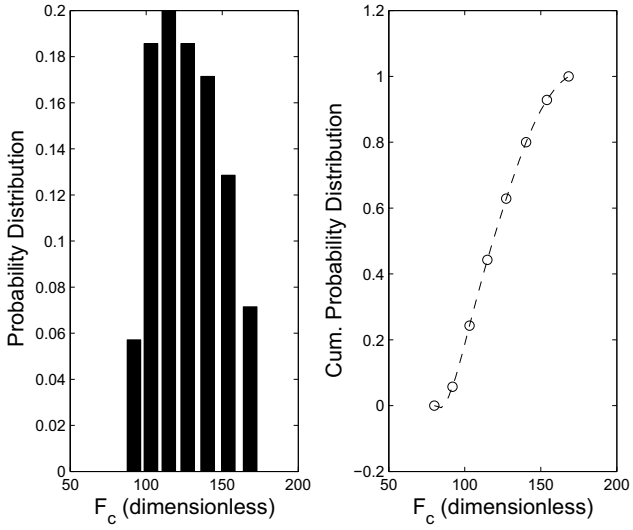

Figure 2.6: The histogram (a) and the cumulative probability distribution (b) for F_c measured on a 1.6 mm diameter and 2.54 mm cylinder having a density of 7800 kg/m^3 with a fluid having a yield stress of 4 Pa. Approximately 70 observations were made. Cylinder axis of symmetry is parallel to the direction of motion.

which have remained unstable. In this case the histogram was skewed toward the lower values of F_c and this finding is representative of all cases tested. The critical values for each experiment are given in these tables in which the uncertainty in the mean is reported at the 95% confidence interval. What is evident is that motion occurs over a range of F_c and variation (standard deviation) in this example is 21% of the mean. It should be noted that the example chosen represents a data set with one of the largest standard deviations. Generally the results where much better. The error in this case stems from the initial positioning of the particle in the centrifuge. A small error is introduced as it is difficult to reposition the

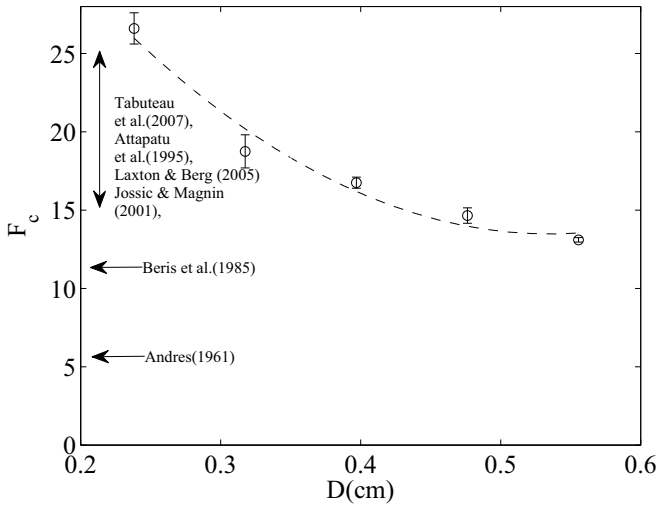

Figure 2.7: Estimate of the critical force required to initiate motion for stainless steel spheres with diameters in the range 2.4 mm$\leq D \leq$ 5.6 mm. The dotted line represents linear regression of the data with a second order polynomial. The arrows represent literature values for theoretical estimates, i.e. Andres (1961); Beris et al. (1985), or experimental works, Attapatu et al. (1995); Tabuteau et al. (2007); Jossic and Magnin (2001); Laxton and Berg (2005). The uncertainty in the estimates are reported at the 95% confidence interval.

particle, with the correct orientation, between trials. As a result, a large number of replicates for each test were conducted to increase our confidence in our estimate of the mean. At this point we turn our attention to the estimates of F_c measured as a function of particle diameter, see Figure 2.7. The first observation that can be made from this figure is that F_c is a strong function of D. When we re-examine the pertinent works in the literature, i.e. Attapatu et al. (1995) and Jossic and Magnin (2001), we conclude that previously reported results were obtained from indirect methods; F_c was determined by extrapolation from measurements of a

slowly translating sphere. The question of "slip" on the surface of the particle was not addressed in this work whilst making this extrapolation. In addition the uncertainty in the estimates given by Attapatu et al. (1995) and Jossic and Magnin (2001) are within the range of variation given in Figure 2.7. From this we conclude that the methods used in the previous literature studies were not sensitive enough to observe this functional relationship. Like Putz et al. (2008) we too must draw the conclusion that the unyielded envelope is not spherical in shape (otherwise it would be independent of D). Our interpretation assumes that Carbopol chains do not adsorb on the particles and do not affect their DLVO interactions or their distance of maximum approach.

Next we turn to the main point of this section and we attempt to demonstrate the fractionation principle using one specific example. Here we create a separation based upon the differences in densities of two spheres having equal diameter. The spheres are placed in a centrifuge at equal radial distances from the axis of rotation and the angular velocity is set. From this we can estimate the force ratio F_1 and F_2 acting on each particle during the experiment. Three different scenarios can be constructed:

1. Both F_1 and F_2 are *less* than the critical force F_c determined in Figure 2.7. In this case both particles remain stably trapped.

2. Both F_1 and F_2 are *greater* than the critical force F_c. Here motion begins for both particles.

3. If $F_1 > F_c > F_2$, particle 2 remains stably trapped while particle 1 moves.

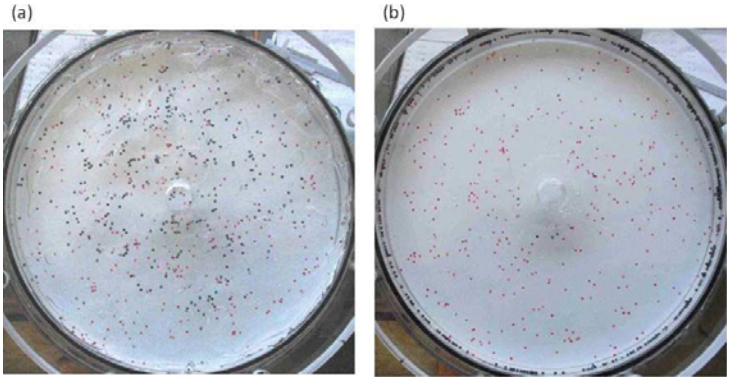

Figure 2.8: A demonstration of the fractionation of a bidisperse suspension of spherical particles. In (a) an image of the suspension is given before the commencement of the centrifuge. (b) is the state of the suspension after the application of the centrifugal force.It should be noted that most of the darker particles are on the periphery of the centrifuge.

Under this case separation has occurred. This is the separation principle

To highlight this last scenario we examine Figure 2.8(a) where we have created a bidisperse suspension of spheres with similar diameters but vastly different densities. The sphere with the larger density is shown in black and that with the smaller density in red. An equal number of each type of sphere is distributed throughout the centrifuge. If the centrifugal force is chosen correctly, as shown in Figure 2.8(b) separation can indeed occur. Here we see that the heavier spheres migrated towards the periphery whilst the lighter ones were held by the gel.

2.3.2 Cylinders

From the previous subsection, we demonstrated that these gels could be used to create a separation of a bidisperse suspension of spheres. As a proof of principle,

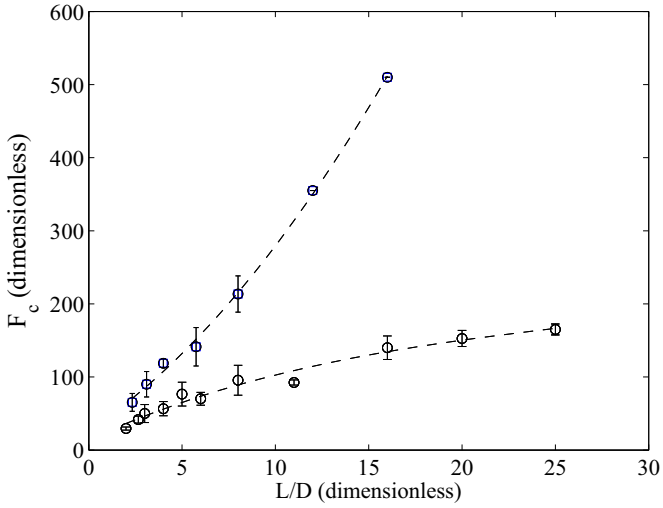

Figure 2.9: Measurement of the critical force ratio F_c to cause motion in isolated cylinders of various aspect ratios. Cylinders oriented perpendicular to the direction of the force are shown as a square (□). Cylinders oriented with their axis parallel to the direction of force are shown as circles (○). The uncertainty in the estimates are reported at the 95% confidence interval.

we showed a nearly perfect separation of a bidisperse suspension of spheres based upon particle density. In this section we continue to build on our understanding of this separation and report on the motion of isolated cylinders in a centrifuge. Cylinders are a more complicated geometry and we suspect that orientation could affect the shape of the unyielded envelope. We present the results in this subsection in a similar manner as to those presented in the previous subsection. First the results for isolated particles are given followed by a number of fractionation demonstration experiments.

To begin, like spheres we measured F_c for a large number of cylinders of differ-

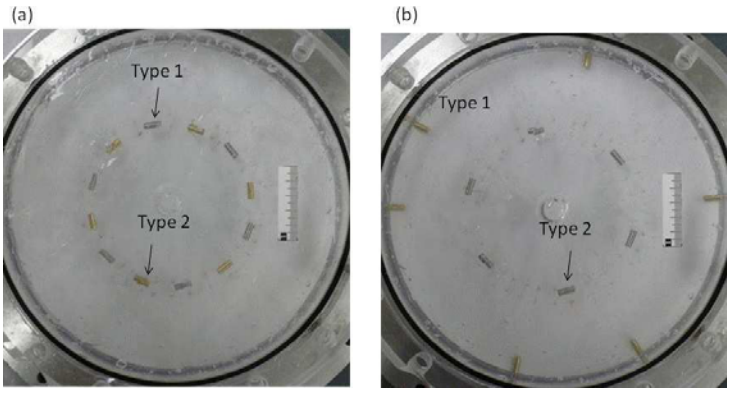

Figure 2.10: A demonstration of the fractionation of a bidisperse suspension of cylindrical particles(similar size, different density). In (a) an image of the suspension is given before the commencement of the centrifuge. (b) is the state of the suspension after the application of the centrifugal force.

ent aspect ratio, diameter, density, degree of curvature, and orientation (measured relative to the application of force). The results for rigid cylinders are shown in Figure 2.9. The first observation that can be made is that with increasing aspect ratio, a larger force is required to initiate motion for the cylinders oriented perpendicularly to the direction of force than those oriented in the parallel sense. We report these two bounds as we feel that any orientation state between these two limits should lie somewhere between these two curves. The second observation that we can see is that for cylinders oriented perpendicular to the direction of the force, F_c was found to vary nearly linearly with the aspect ratio of the particle. The third observation that can be made from Figure 2.9 is that for particles oriented parallel to the direction of the force, at larger aspect ratios, F_c seemingly approaches a constant value. This latter finding, however, should be confirmed

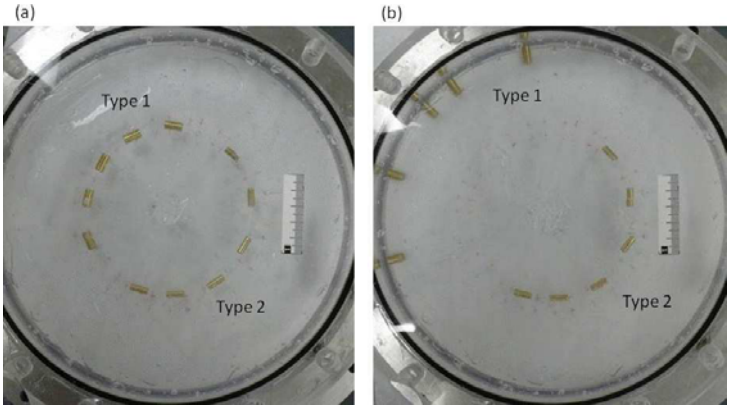

Figure 2.11: A demonstration of the fractionation of a bidisperse suspension of cylindrical particles(similar length and density, different diameter). In (a) an image of the suspension is given before the commencement of the centrifuge. (b) is the state of the suspension after the application of the centrifugal force.

with larger aspect ratio particles. In the next stage we attempt to demonstrate this principle by creating separations based upon either diameter or density. In Figure 2.10 the cylinders in this case have equal diameter and length but have two different densities. The lighter colored rod has the larger density. In Figure 2.10-(a) an image of the particles is given before the commencement of the centrifuge. In Figure 2.10-(b) the state of the suspension after the application of the centrifugal force is shown. It should be noted that all of the denser particles moved to the periphery while the less dense ones remained trapped. In a similar manner we demonstrate a fractionation based upon diameter. In Figure 2.11, the cylinders in this case have equal density and length but have two different diameters. The larger diameter rods are located in the upper left quadrant of the image in 2.11-(a). In Figure 2.11-(a) an image of the particles is given before the commencement of

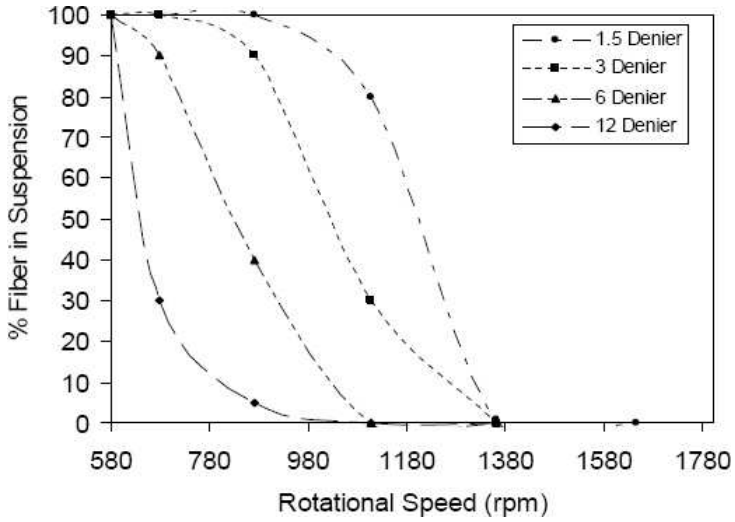

Figure 2.12: The fraction of nylon particles remaining stably trapped after the application of a centrifugal force. The fibres were randomly oriented initially. The nylon particle were of equal length. Denier is a representation of the diameter of the fibre.

the centrifuge. Figure 2.11-(b) is the state of the suspension after the application of the centrifugal force. It should be noted that all of the larger diameter particles moved to the periphery while the smaller diameter ones remained trapped. With the principle of separation shown for isolated particles, we attempt to perform a demonstration of this principle with particles better representing papermaking fibres. We do so in two separate studies with nylon fibre suspensions of various length and denier[6]. As the density of these particles are so small in comparison to the test particles used, the separation was conducted in the higher speed centrifuge. In the first series of tests, see Figure 2.12, nylon fibre suspensions of various de-

[6]Denier is unit of measurement of linear density of textile fiber mass- calculated as one gram per 9000 meters. It is related to diameter of the fibre.

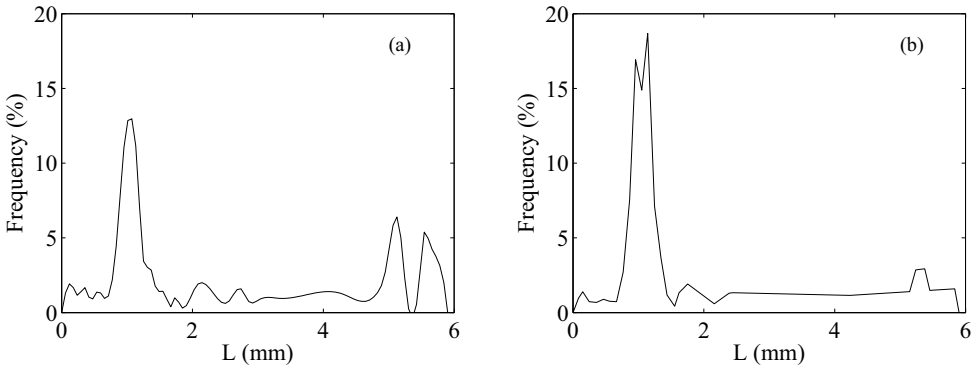

Figure 2.13: The separation of Nylon fibres of equal diameters with different lengths. (a) The fibre length distribution of the sample initially. (b) The fibre length distribution of the stably trapped fibres after treatment with the centrifuge at 1200 rpm.

nier were suspended in a Carbopol gel and rotated at increasing rpm. The portion of the fibres which were stably trapped were recovered and the number of fibres determined using a Fibre Quality Analyzer (www.optest.com). The orientation of the fibres was not controlled in this experiment and should be considered to be randomly distributed. The results indicate that the threshold required to cause motion increased with increasing denier of the particle. What is evident in this figure is that a complete separation of say a 1.5 denier particle from a 12 denier particle could be achieved at 980 rpm. In the second set of tests, a suspension of equal denier nylon fibres but with different lengths are separated in a centrifuge, see Figure 2.13. Here nearly complete separation was achieved at 1200 rpm.

Following the purpose of fractionating papermaking fibres, having a proof on fractionation using Nylon fibres, we tried separating wood fibre in the Carbopol under centrifugal force. To do so, we repeated the same process of Nylon fibres

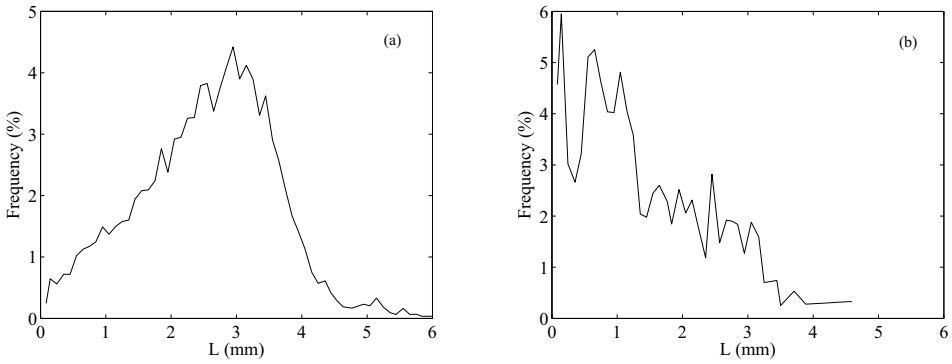

Figure 2.14: The separation of a softwood bleached Kraft pulp based upon length.(a) The fibre length distribution of the sample initially. (b) The fibre length distribution of the stably trapped fibres after treatment with the centrifuge at 2900 rpm.

and chose semi bleached kraft pulp and made the pulp solution by adding the fibres into Carbopol. The result presented here is for the fibre concentration of 0.16% and fluid yield stress of approximately 1 Pa (Figure 2.14).

From Figure 2.14 one can see how the length distribution changes after applying the centrifugal force. The length weighted average[7], L_w of the initial sample was 2.56 mm with the maximum distribution of fibres around 3 mm, while after being exposed to centrifugal force the L_w has dropped to the value of 1.44 mm with maximum distribution around 1 mm.

2.4 Limitations - Applications to Real Systems

At this point we are trying to build an understanding of the limitations of the proposed separation principle. Thus far we have studied ideal systems both in terms

[7]Length-weighted mean fiber length is defined as $L_w = \frac{\Sigma[(n_i L_i)L_i]}{\Sigma(n_i L_i)}$.

of the definition of the properties of the particles and in terms of the concentration regimes tested, i.e. dilute. A small discussion of each is given below.

We begin to test the assumption regarding the shape of papermaking fibres by including the effects of kink or curl into the particle. To do so we modified our system by bending the cylindrical rods and then measuring F_c in the manner described above, see Figure 2.15. similar to the rigid bars, the force is a function of L/D. What is evident is that F_c is quite sensitive to the bend in the rod.

In addition, the size of the unyielded envelope places an upper limit on the concentration of the suspension which can be used. Here, the separation principle will be diminished if the unyielded zones of adjacent particles overlap. Just like with particle flow with Newtonian fluids, this represents a long-range hydrodynamic disturbance. At this point we attempt to estimate the size of the unyielded zone based upon our experimental results. To do so we conducted a series of tests where spheres of a known diameter which were placed at equal R in the centrifuge but at different interparticle spacings. The isolated particle results could be obtained when the interparticle spacing was greater than one particle diameter.

At this point it is difficult to say if this principle will be more efficient than existing fractionation technologies, i.e. hydrocyclones or pressure screens, as the work was conducted batch wise, at low concentrations and with primarily idealized particles. Further work is required to ascertain properly the efficiency and limitations of this principle when scaled-up to a continuous operation and compared to existing technologies. The results of this study are not limited to the use of Carbopol-940. We have used this yield stress fluid convenient as we have

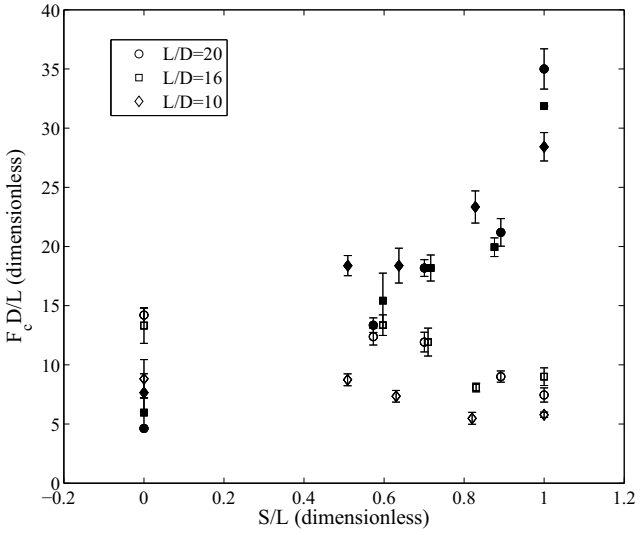

Figure 2.15: Measurement of the critical force ratio F_c to cause motion in isolated bent cylinders. The measurements were conducted both as function of aspect ratio and degree of kink S/L. Particles oriented perpendicular to the direction of force as shown as filled symbols. Particles oriented parallel to the direction of force are unfilled symbols. The uncertainty in the estimates are reported at the 95% confidence interval.

experience with it. Other yield stress fluids could be employed.

Chapter 3

Application-Part 1: Fractionation of Papermaking Fibres

3.1 Introduction

[1] The focus of the present chapter is to apply the novel fractionation technique presented in the previous chapter to papermaking fibre suspensions. Fractionation implies particle sorting in which the suspension is separated into fractions with similar physical properties. There are essentially two methods to fractionate pulp fibres industrially: pressure screens and hydrocyclones. Sloane (2000), Julien Saint Amand and Perrin (1999) and Olson et al. (1999) indicate that in pressure screens fractionation occurs based upon fibre length and flexibility. Hydrocy-

[1] This chapter is published in: **Madani A.**, Olson J.A.,Martinez D.M., and Fung, A. (2010). "Novel methods to characterize and fractionate papermaking fibres" Nordic Pulp and Paper Res, Vol. 25, Issue 4, pp. 448-455.

clones, on the other hand, are more versatile and fractionation proceeds based upon fibre length, specific surface or coarseness[2] (Bliss (1984); Karnis (1997); Ricker and House (1984); Wood and Karnis (1977, 1979); Kure et al. (1999); Li et al. (1999); Park et al. (2005)).

It is widely known that fractionation of papermaking fibre suspensions is particularly difficult as there are distributions in both fibre length and coarseness. This implies that fibres of vastly different dimensions may have similar masses over surface area. In a fairly crude way, one can argue that papermaking suspensions are composed of a broad spectrum of coarsenesses from the change in growing season. Vomhoff and Grundström (2003) report that papermaking suspension can indeed be separated into early and late -wood streams through an extensive number of hydrocyclones. They report however that the efficiency of the process is low. Similar results were also reported by Paavilainen (1992); Malm (1967); Coppick and Brown (1963). Our work is motivated from this study and we investigate a methodology which may be more efficient.

In this chapter, we evaluate the utility of this method for papermaking fibre suspensions. The work is conducted in two separate yet complimentary studies. In the first study, we characterize the range of physical properties of the particles in the suspension. In this section we report a novel methodology to characterize the fibre suspension. As indicated in the previous chapter, the fractionation efficiency of the novel technique depends upon the mass, as well as the aspect ratio distri-

[2]Fibre coarseness is defined as mass per unit length and in a very crude manner is a measure of the fibre wall thickness.

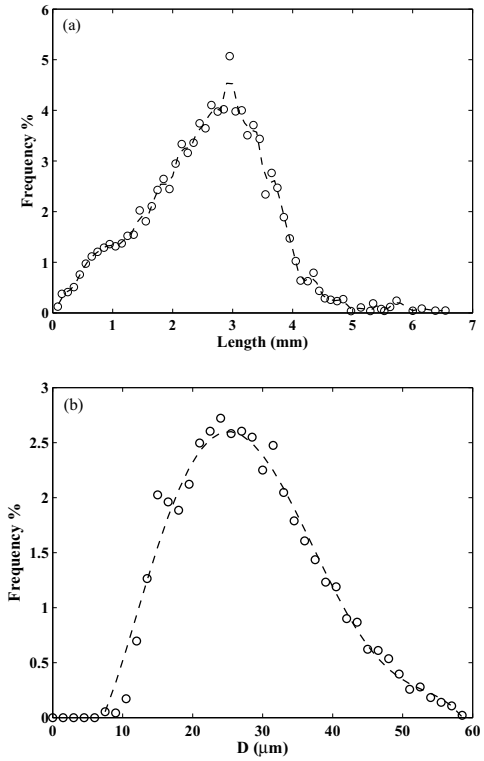

Figure 3.1: (a)Fibre length and (b) fibre width distribution for SBK pulp used in this study (The length reported here is the length weighted average $L_w = \sum(n_i L_i)/\sum(n_i L_i^2)$).

butions of the fibres in the suspension. Here we demonstrate qualitatively why it is possible for this new fractionation method to separate based upon both length and coarseness. In the second study we demonstrate the utility of the separation by examining fractionation of an SBK pulp as a function of initial consistency, fractionation time, and initial fibre length distribution.

3.2 Characterization of the Particle Suspension

In this section we characterize the physical properties of semi-bleached kraft pulp (SBKP) through measurements of the length (L), width (D), aspect ratio (L/D) and coarseness (C). What is unique in this work is that we propose a methodology to determine the relationship between C and L.

To begin, we report the length and width distribution in Figure 3.1. These were obtained through a routine analysis with a Fibre Quality Analyzer (FQA, obtained from www.optest.ca). The trends displayed in this figure are typical for most papermaking suspensions and we report a length-weighted mean fibre length and width averages of $2.401(\pm 0.018)$ mm and $29(\pm 9.8)$ μm, respectively. In addition to these, we report the fibre aspect ratio distribution. This parameter is not commonly reported from the FQA but can be obtained through post-processing of the output file from this device. Here data of the length and diameter of each particle analyzed is available. We post-processed this file and present three measures of the aspect ratio. In Figure 3.2 *a* and *b*, the raw data is reported. We see some slight discernible trend in the data. Finally to help ascertain if any relationship exists between length and diameter, we sort the raw data into a number of length bins and average the width of the fibres in each bin, see Figure 3.2 *c*. Here we report 5 bin sizes, i.e. fibre lengths which are found to fall within 0-1 mm, 1-2 mm, 2-3 mm, 3-4 mm, and 4-5 mm. Following this we can define a simple relationship between the length and diameter of the fibres in the suspension. Using linear regression, we show that the diameter of the fibre is related to its length

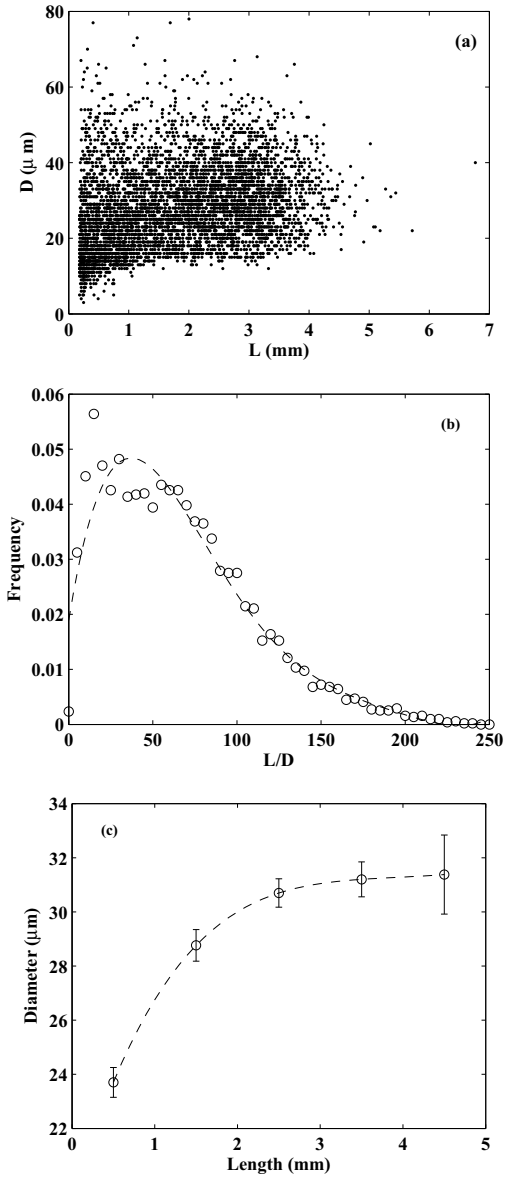

Figure 3.2: Characterization of the aspect ratio of the SBK pulp used in this study. (a) raw data from the Fibre Quality Analyzer (b) the frequency of the aspect ratio of the initial fibres used in the study and (c) a proposed relationship between length and diameter after averaging. The error bars represent the 95 % confidence intervals.

using an equation of the form

$$D = \frac{L}{a_o L + a_1} \tag{3.1}$$

where a_o and a_1 are found to be 30.5 mm^{-1} and 5.9 respectively with L and D in mm. This equation can be rearranged to show that the aspect ratio of the fibre increases linearly with fibre length. We find that the aspect ratio ranges from 5.9 for smaller particles to approximately 100 for fibres which have a length of approximately 3 mm. We will discuss the significance of these findings in term of fractionation shortly. We now turn our attention to the main findings in this section, that is a methodology to estimate the relationship between fibre length and average coarseness. This relationship is traditionally obtained by first fractionating the suspension and then measuring the coarseness and length of each fraction. We have repeated this approach using Bauer-McNett to fractionate fibres and the results are shown in table B.2; the fibre length distributions of some of the fractions are also displayed in Figure 3.3.

In this table, we report the average coarseness $\bar{C_j}$ and length L_j of 5 different fractions of the original sample.The uncertainty in the estimates is reported as standard deviation determined from three replicate tests. It is important to note that in order to achieve a better fractionation a nonstandard procedure was followed and the residence time of the fibres in the Bauer-McNett was increased and then the fibres in each mesh were collected and they were fractionated two more times to make sure the samples are statistically different and a good fractionation

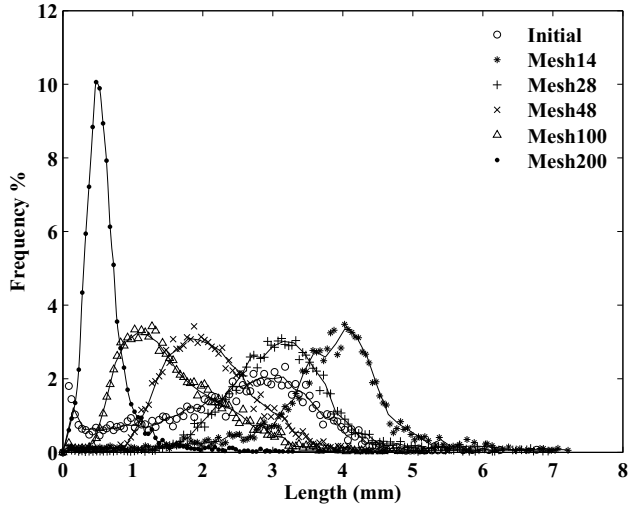

Figure 3.3: Characteristics of the Bauer-McNett fractionated samples. The fibre length distributions of each sample are given in the figure.

is achieved. At this point we would like to refine this estimate between $\bar{C_j}$ and length by including the effect of the fibre length distribution. By definition, the average coarseness of sample j, is determined from the total mass M divided by the total length of fibre, i.e

$$\bar{C_j} = \frac{M}{N \sum_{i=1}^{n} p_{ji} L_i} \tag{3.2}$$

where N is the total number of fibres in the sample; and n is the number of fibre length classes reported by the fibre quality analyzer. The matrix p_{ij} represents the probability of finding a fibre of length L_i in sample j. This value is obtained directly from the FQA analysis of the pulp sample.

The key to this analysis is that the average coarseness of each measured sample

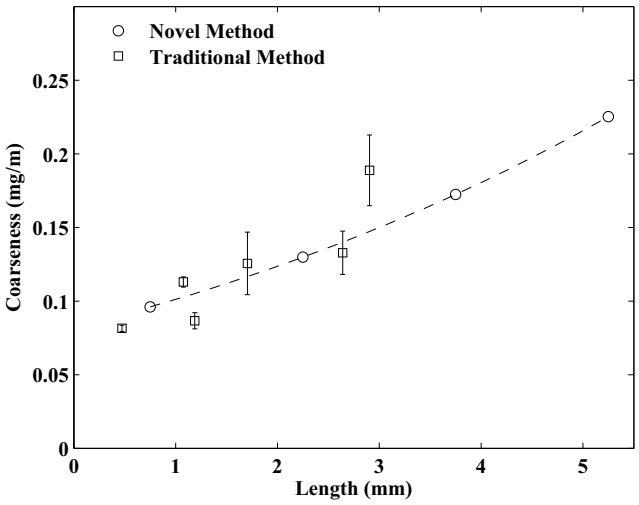

Figure 3.4: Coarseness values of samples directly obtained from Bauer-McNett and values calculated using regression method. The bin sizes and average values of coarsenesses for each bin are reported in the table B.3. The errors represent standard deviation.

$\bar{C_j}$ is uniquely related to the coarseness C_i of fractions which comprises the entire suspension, i.e.

$$\bar{C_j} = \frac{\sum_{i=1}^{n} p_{ji} L_i C_i}{\sum_{i=1}^{n} p_{ji} L_i} \tag{3.3}$$

The numerator is related to the mass of the fibres in the sample. This relationship can be rearranged to form the following linear system

$$\mathbf{Ax} = \mathbf{b} \tag{3.4}$$

where

$$\mathbf{A} = \begin{bmatrix} p_{11}L_1 & p_{12}L_2 & \dots & p_{1n}L_n \\ p_{21}L_1 & p_{22}L_2 & \dots & p_{2n}L_n \\ \vdots & \vdots & \ddots & \vdots \\ p_{m1}L_1 & p_{m2}L_2 & \dots & p_{mn}L_n \end{bmatrix} \mathbf{x} = \begin{bmatrix} C_1 \\ C_2 \\ \vdots \\ C_n \end{bmatrix} \mathbf{b} = \begin{bmatrix} \bar{C_1} \sum_{i=1}^{n} p_{1i}L_i \\ \bar{C_2} \sum_{i=1}^{n} p_{2i}L_i \\ \vdots \\ \bar{C_m} \sum_{i=1}^{n} p_{mi}L_i \end{bmatrix} \quad (3.5)$$

and m is the total number of samples.To solve this set of equations two sub cases need to be considered. The first sub case represents a mathematically determined system of equations in which the number of fibre-length classes (n) equals the number of samples (m). Under this condition the coefficient matrix $\mathbf{A}$ is square so the solution can be written as

$$\mathbf{x} = \mathbf{A}^{-1}\mathbf{b} \quad (3.6)$$

as long as the matrix $\mathbf{A}$ is not singular. The second case represents the overdetermined case where $m > n$ and there is no solution that satisfies all the equations strictly. In this case a least-square error (LSE) method has been used (Chapra (2006)).

The results of this are presented in Figure 3.4 with $m = 18$ and $n = 4$. These 18 samples were obtained from pulp fractionated from Bauer-McNett and the original pulp. In this case we collected 5 fractions, plus the original pulp, and performed three replicate tests. The coarseness values reported in Figure 3.4 are listed in table B.3 . The first observation that can be made from this result is that the LSE

approach gives values similar to that of the more direct fractionation approach. The displayed trend however is smoother as there is less scatter in the data. We interpret this result as an indication that thicker wall latewood fibres, on average, are more prevalent in the large fibre-class bins than earlywood fibres.

At this point we attempt to relate these findings to the potential of this novel method to fractionate. To begin, as indicated in the previous chapter that the force required to initiate motion in this gel is related to both the mass and the aspect ratio of the fibre. With regards to separation based upon length, the results presented in Figure 3.4 indicate that fibre coarseness increases somewhat linearly over the range of the length reported (similar results have been observed in the literature (Lapierre et. al. (1997))). This indicates that the mass of the particles, m_p must vary according to

$$m_p = C_i L_i \propto L_i^2 \tag{3.7}$$

We interpret this result to indicate that longer fibres will move sooner under the action of a centrifugal force than shorter fibres. In fact, since mass is related to the length of the fibre squared, we argue that this method should be quite efficient in removing long fibres from short ones. With regards to fractionation based upon coarseness, we examine the results in Figure 3.2. Here we find that the aspect ratio of the fibre increases with increasing length initially; fibres which have a length greater than 2 mm have essentially the same diameter. From this we argue that

the only means to separate based upon coarseness is to fractionate a suspension with the fibres of the same initial length. In this case the fibres should have similar aspect ratios but have differing masses. Both of these speculations will be tested in the next section.

3.3 Separation of Papermaking Fibres in a Gel

In the previous section, we characterized the papermaking suspension by measuring the length, diameter and aspect ratio distributions as well as developing a more refined estimate of the relationship between coarseness and fibre length. In this section we will attempt to fractionate this suspension in two distinct separation demonstrations. In the first demonstration, we examine separation based upon length of the original pulp suspension and examine the effects of time and consistency on the fractionation event. In the second demonstration we attempt to assess the sensitivity of the methodology by performing separations on initially fractionated suspensions. Here we fractionate suspensions based upon coarseness for fractions with nearly equal fibre length.

3.3.1 Experimental Details

In this work we measured the angular velocity required to initiate motion of a papermaking fibre suspension in a yield stress fluid under the action of a centrifugal force. The centrifuge used was a Universal Model UV centrifuge at rotational rates of up to 3500 rpm. 50 ml plastic tubes with 3 cm diameter were used as the fluid containers inside the centrifuge. The moment arm of the centrifuge was 15

cm. The main fluid used in this study was Carbopol-940 obtained from Noveon. In this work a 0.16 % (wt/wt) Carbopol solution was prepared using DI water and then neutralized using a dilute NaOH solution. The density of the resulting solution was that of water. The resulting gels were degassed and then allowed to rest overnight. Rheological characterizations were performed at room temperature in a cone and plate flow geometry on a Bohlin rheometer. Shear sweeps were performed in controlled strain mode typically in the range of 1 10^{-2} s^{-1} to $1s^{-1}$ in order to determine the yield stress, a typical rheogram of the fluid is shown in Figure 2.4.

A number of different studies were performed in which time, consistency, and initial fibre aspect ratio distributions were varied. The pulp in use was a semi-bleached kraft pulp (80 % Pine and 20 % Spruce-Fir). In our initial study, a 0.1 % (wt/wt) pulp consistency prepared in Carbopol was placed in a test tube in the centrifuge. The centrifuge was quickly accelerated up to 3500 rpm and then held at this speed for varying lengths of time. After separation, the top two third of the test tube, containing particles which did not move under the action of the centrifugal force, were recovered. We call these fibres the "retained" fibres as they did not move under the application of the force. The retained suspension was then filtered and its length distribution determined using the FQA. From this, we estimate the mass fraction m_i of each class of fibres using this and the data given in Figure 3.4.

$$m_{ji} = \frac{p_{ji} C_i L_i}{\sum_{i=1}^{n} p_{ji} C_i L_i} \tag{3.8}$$

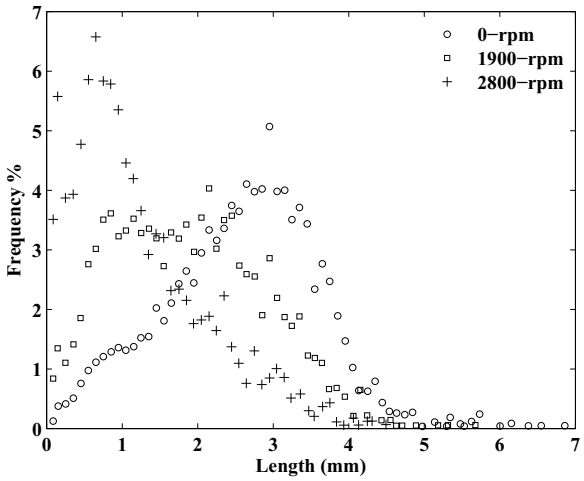

Figure 3.5: Phenomenological demonstration of the fractionation of a 0.08 % SBK pulp under the action of force for 12 min.

where *j* is the sample number and *i* is the length class.This procedure was repeated but in this case we examined the effect of concentration. Here four concentrations are examined, namely, 0.01, 0.07, 0.28, and 0.56 % where the separation proceeded for 10 minutes at increasing rotational rates up to 3000 rpm.

In the second study we examined the sensitivity of the separation method by separating suspensions which have already been fractionated once using a Bauer-McNett. Here we re-fractionate Mesh 14 retained fibres in this novel technique and measure the change in coarseness.

Note that since the yield stress of the Carbopol gel varies with polymer concentration, the fibres were removed from the gel by first dilution (in order to diminish the yield stress) and then filtered.

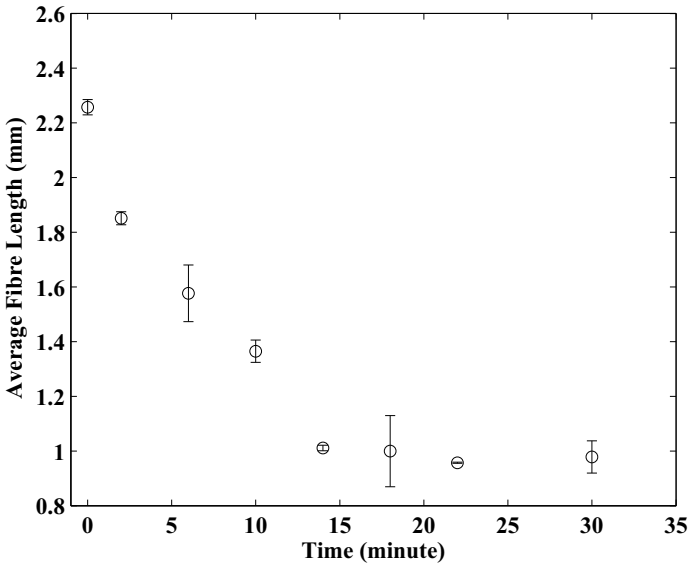

Figure 3.6: The change in average fibre length of the retained fibres.

3.3.2 Results

To help understand the behavior of this fractionation technique, we present first a phenomenological result on the differences in fibre length distributions as a function of rotational rates, see Figure 3.5. What is shown in the figure is the fibre distribution of the suspension retained at the top of the test tube. What is evident in this figure is that the larger, and somewhat heavier particles move towards the bottom on the test tube, leaving the smaller, lighter particles, at the top of the test tube. This procedure was repeated for increasing centrifugal times, see Figure 3.6. Interestingly, the average length diminished somewhat linearly with increasing time for approximately 15 minutes. We attribute this to represent the migration time of the particles under the application of the force. From this graph

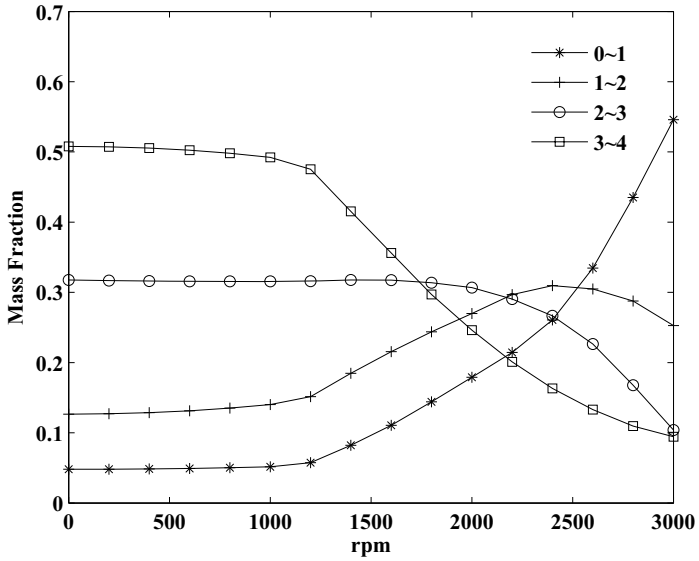

Figure 3.7: Variation of fibre mass in each bin as rpm is increased.

it can also be concluded that it is possible to get a required fibre length only by controlling the time the fibres are under the applied force.These tests were performed at 0.1 % consistency and a rotational speed of 3500 rpm. A demonstration of fractionation based upon length is shown in Figure 3.7. It should be noted that the y-axis in this case represents the mass fraction of each length-class of fibre and was determined using equation 3.8. To help interpret this figure, at any rpm, the sum of the mass fractions should equal one. The first observation that can be made from this figure is that initially the long fibre fraction represented over 50 % of the mass of the sample. After approximately 1200 rpm, the long-fibres migrated towards the bottom of the test tube. This caused enrichment in the smaller fibre length classes. After approximately 3000 rpm the retained suspension contained

mostly short fibres.

The effect of consistency is shown in Figure 3.8. The results are presented in terms of the normalized mass fraction. This represents the mass fraction at a certain rpm divided by the corresponding mass fraction of the fibre class in the original suspension. From these results we observe that the fractionation indeed occurs over the consistencies measured as the relative changes in fibre distributions of the retained samples are approximately the same. These results show that by increasing the consistency, the fibre motion starts in lower rotational speeds. This result however should not be interpreted to imply that the fractionation mechanism applies over all consistencies. Although not measured, it should be noted that the yield, i.e the total mass of suspension retained, diminished dramatically with increasing consistencies. Further work is required to understand the effect of consistency.

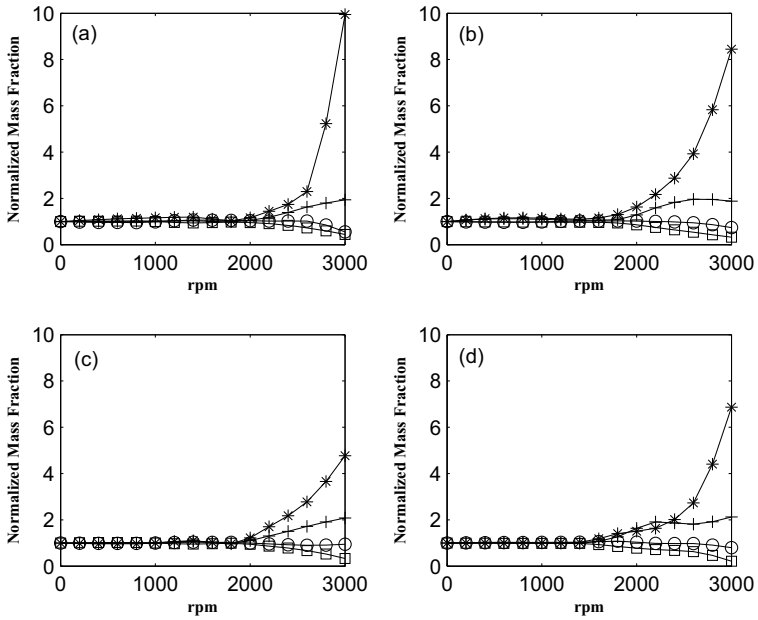

Figure 3.8: Normalized mass fraction of different bin sizes. The $*, +$,o and $\square$ represent bin sizes $0-1$, $1-2$, $2-3$ and $3-4$ mm correspondingly. Figure (a) represents 0.01% , (b) 0.07% , (c) 0.28% and (d) 0.56% pulp consistency.

Finally, we examine the sensitivity of this technique and measure the change in coarseness for particle retained on the Mesh 14 screen of a Bauer-McNett, see Figure 3.9. In this study we also measured the coarseness of the material which migrated to the bottom of the centrifugal test tube. The two third of the sample collected at the top of the test tube is called as the top and the remaining sample collected at the bottom of the test tube is called bottom. The first observation that can be made is that with increasing rotational speeds, the average coarseness of the retained particles diminishes. This reflects the fact that although the particles

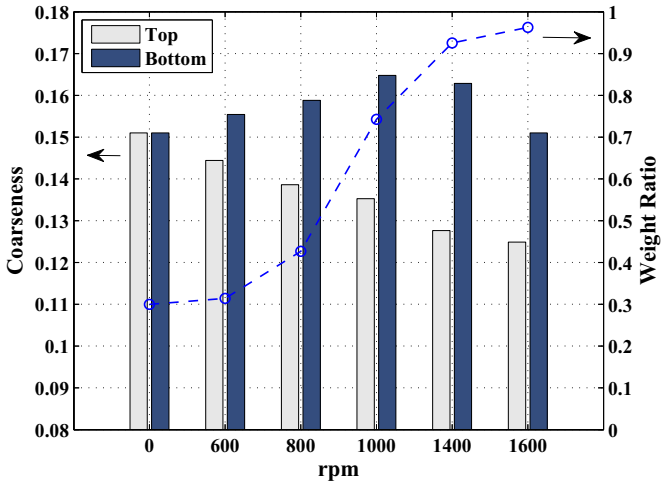

Figure 3.9: Fractionation of Mesh 14 fraction based upon coarseness (0.05% fibre consistency).

have nearly the same length (3.6 mm), the fibres have a population distribution in cell wall thickness. This results from the growing seasons in the tree(early wood and late wood). What is also evident in this figure, is that the average coarseness of the migrated material first increases, and then subsequently decreases, as more particles move under the action of the force. In this case at 1000 rpm the coarseness value of the retained sample is 0.135 compared to the value of 0.165 for the settled value. The weight ratio is the ratio of the mass of the fibre at the bottom over the total initial mass of the fibre in each sample. Plotting these two curves together helps to achieve a better understanding of the efficiency of the separation. Based on the weight ratio, at 1000 rpm 20 % difference in coarseness was observed while 35 % of the sample mass has not moved yet and it shows good yield efficiency.

3.4 Summary and Conclusions

In the first part of this work we have introduced a new technique to process the statistical results that are obtained from FQA. That is by writing a mass balance for each sample and using the relation between length and diameter of the fibres we generated a tool to get a better estimate of fibre coarseness. This better estimate is a representative of average coarseness in smaller length distributions which gives us better insight into the morphology of the fibres compared to the average coarseness value over the entire fibre length distribution that was used before. The results here indicate that the mass of the fibre increases with L^2. In the second study we applied the fractionation technique proposed in chapter 2 and demonstrated fractionation based upon either length or coarseness.

Chapter 4

Application-Part 2: Fractionation of Microfibrillated Cellulose (MFC)

4.1 Introduction

[1] As another application of the proposed fractionation technique, in this chapter we examine the fractionation of microfibrillated cellulose (MFC) and its effect on the tensile index and elongation of paper.

In the first part of this chapter, we compare the fractionation of commercially available MFC using multiple stages of traditional fractionation unit operations, namely a hydrocyclone and a pressure screen, to our novel technique based upon the control of the threshold for motion in a weak gel. In the second part of the

[1] This chapter is published in **Madani A.**, Kiiskinen, H., Olson J.A., and Martinez D.M., (Accepted). "Fractionation of microfibrillated cellulose and its effects on tensile and elongation of paper" Nordic Pulp and Paper Res. Journal.

work, composite paper samples are formed by addition of fractionated and non-fractionated MFC to chemical wood pulp and the strength of the resulting composites are studied.

The potential of nanotechnology is far reaching. One promising area is the development of nanocomposite materials that are light-weight with high-strength. In particular, microfibrillated cellulose (MFC) reinforced polymer composites have recently found applications in the automotive, aerospace and construction industries due to their strength as well as their active or "smart" properties (Hubbe et al. (2008); Azeredo (2009)). One of the remaining open questions is that of a reliable manufacturing method to fractionate or separate MFC from cellulose fibre for large scale manufacturing purposes. This class of problem is gaining interest rapidly in the Pulp & Paper industry.

Before we discuss the relevant separation techniques available, it is instructive to first review the source of MFC and its potential benefits on the physical properties of paper. It is well known that an excellent source of MFC is the cellulose fibrils found in the walls of either hardwood vessel elements and softwood tracheids or pulp fines from chemical pulps. Turbak et al. (1983) has explained the process that results in production of MFC in details. Once these elements have been separated and processed to create MFC, small additions of this to traditional polymer-reinforced composites have been shown to increase the elastic modulus more than 1000 times (Hajji et al. (1996); Dufresne et al. (1997); Jordan et al. (2005)). For MFC reinforced paper, the application which motivates the present study, Iwatake et al. (2008) demonstrates a 25 % increase in the tensile

strength at a 10 % (wt/wt) MFC content.

The MFC recovered from most pulping operations has an inherent length distribution. It is commonly known that the length and aspect ratio distributions of the reinforcing MFC dramatically affect the strength properties of the resulting composites (Hubbe et al. (2008); Dubief et al. (1999); Azizi Samir et al. (2005)). The motivation of the work stems from the need to remove the larger particles, or fibrils, from MFC gels to improve its inherent properties. A number of unit operations currently exist for fractionation purposes, i.e. hydrocyclones and pressure screens, which are able to separate papermaking fibre suspensions, but efficiency of these processes known to be low as discussed in chapter 3.

As a result, in this chapter we report on the fraction of a commercially-available MFC suspension in a sequence of hydrocyclone and pressure screening steps, as well as in a novel technique introduced in previous chapters. The novel methodology involves centrifugation in a viscoplastic carrier fluid. Following this we assess the reinforcing ability of these purified samples by assessing the tensile strength of MFC reinforced paper. This would follow a similar approach to the work of Nakagaito et al. (2009) which produced MFC-reinforced composite sheets in a process similar to papermaking. Their results show increase in physical properties of produced composite as MFC is added.

4.2 Methods and Materials

Microfibrillated cellulose (MFC) samples, obtained from JRS (www.jrs.de), were used in this work(with the commercial name of NFC). The samples had an average

fibre length of 221 μm as determined using an L & W STFI Fibremaster (Karlsson (1999)). The MFC sample was then fractionated using one of three techniques.

In the first technique, the MFC was fractionated using four hydrocyclone stages. Here we employed a C-1201 Y Microspin polypropylene hydrocyclone (www.natcogroup.com) with 10mm diameter and operated at 5 bar at a feed flow rate of 4.2 lpm; the initial consistency was set at 0.2 % and accept to reject ratio was set to 6 to 4. After each pass, the reject fraction was collected, its fibril length distribution measured, and then re-fractionated by passing it through the hydrocyclone again. As reported by Paavilainen (1992); Bliss (1984) and Wood and Karnis (1977, 1979), in small size hydrocyclones, the long fibres are collected in "accept" and short fibres leave the device from "reject". In normal conventional size hydrocyclone an opposite trend has been observed (Kure et al. (1999); Li et al. (1999); Park et al. (2005)).

In the second technique we employed a Metso FS-03 pressure screen to fractionate the initial MFC sample. Here, we collected the accept and progressively fractionated the sample by passing it through screens with progressively smaller slot sizes, namely 0.13, 0.09 and 0.06 mm. It should be noted that for traditional papermaking suspensions fractionation generally proceeds with screens operating with screen baskets with holes. In our cases the slotted screen baskets are extremely small and we anticipate some fractionation, albeit not optimal. To compensate for this, in total five stages of screening were performed and we screened the sample through the smallest slot size three times. The screen was operated with five different initial concentrations, which were 0.1 %, 0.3 %, 0.5 %, 0.6 %

and 1 %, with a foil type rotor rotating at 3500 rpm and at a reject ratio of 60 %. After each step the collected samples were diluted to reach the minimum required volume of 15 L. As a result, along the stages the samples became very dilute and effect of initial concentrations became insignificant.

The last set of fractionation experiments was based on controlling the criteria of motion of particle suspended in a weak gel during centrifugation. Here an Eppendorf 5804 centrifuge was used with six 50 mL cylindrical containers and the rotational velocity up to 5000 rpm. In the experiments a 0.16 % (wt/wt) Carbopol solution (Noveon) was dissolved gently in DI (deionized) water and then neutralized using NaOH solution. The resulting fluid was a clear fluid with density of water and a yield stress of approximately 1 Pa. The MFC suspension was then mixed into the Carbopol solution and subjected to a prescribed rotational rate; four different initial concentrations were tested, i.e. 0.1 %, 0.2 %, 0.4 %, and 0.6 % (wt MFC/wt suspension). The top two third of the samples in each test tube were collected as fractionated MFC.

Finally, the fractionated MFC (the retained fraction) was mixed into a chemical pulp (bleached hardwood) at 4 different mass fractions (0, 5, 10 and 15 %). Standard handsheets (Scandinavian SCAN-C standard) were then formed using both initial and fractionated MFC and the tensile strengths of the paper samples were evaluated.

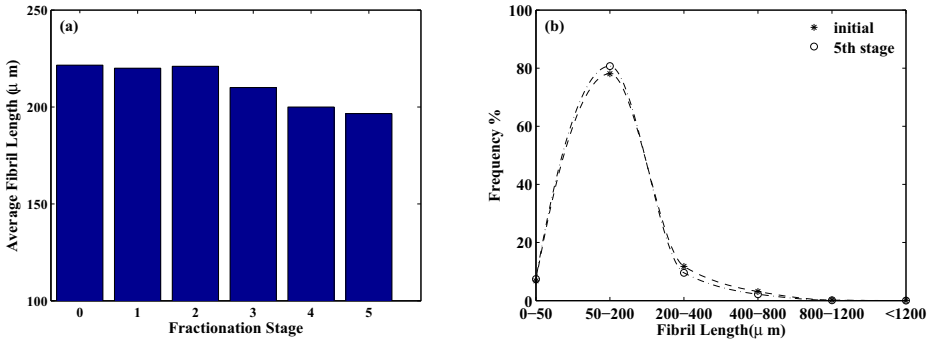

Figure 4.1: Fractionation of a 0.1 % MFC suspension after five stages in a pressure screen. In each stage the accept stream was fed to the subsequent screen. The sizes of the slots in each fractionation stage are as follows: stage 1 - 0.13 mm, stage 2 - 0.09 mm and stages 3-5 - 0.06 mm. In panel (a), the average fibril length is shown. Stage 0 represents the initial fibril length distribution. In (b) a representative fibril length distribution is shown initially and after the fifth stage of separation.

4.3 Results and Discussion

The results of the fractionation studies are shown in Figure 4.1 and Figure 4.2. The first observation that can be made from these figures is that the pressure screen was relatively ineffective in removing the larger size particles in comparison to the other techniques. The fractionation in the pressure screen was attempted over a number of different initial concentrations and we find almost identical fractionation performance due to dilution of the samples. Caution must be used in interpreting these results as we employed slotted screen baskets; a more efficient fractionation may have occurred with screen baskets with holes. This speculation needs to be confirmed as to the best knowledge of these authors, no results are available in the literature indicating the efficiency of fractionation of MFC in

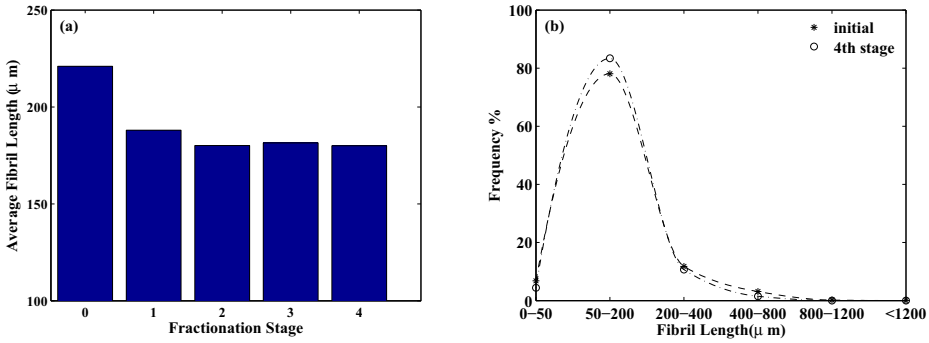

Figure 4.2: Fractionation of a 0.2 % MFC suspension after four stages through a hydrocyclone. In each stage the reject stream was fed into the subsequent hydrocyclone. In panel (a), the average fibril length is shown. Stage 0 represents the initial length distribution. In (b) a representative length distribution is shown initially and after fourth stages of separation.

pressure screens. As a result we display only one result which is representative of all cases tested. The second observation that can be made from these results is that the average fibril length diminished from 221 μm to approximately 180 μm after four fractionation stages in the hydrocyclone, see Figure 4.2. Finally, the largest reduction of fibril length was found using the gel fractionation technique (Figure 4.3); we observed very efficient fractionation as only one stage of this technique was used for all concentrations tested. The variation of fibril length distribution and frequency is shown in Figure 4.3 for 0.1 % fibril consistency. It is important to note that increasing the fibre consistency in the gel fractionation has a significant effect on the fractionation result and as the consistency is increased, more fibrils are moved to the bottom of the test tube and the yield efficiency (remaining mass in the system) reduces.

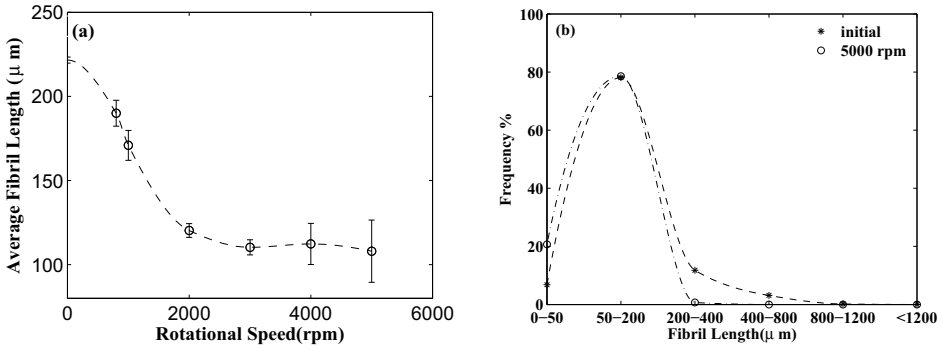

Figure 4.3: Fractionation of a 0.1 % MFC suspension after centrifugation at different rotational rates. In panel (a), the average fibril length is shown as a function of rotational rate. In (b) a representative fibril length distribution is shown initially and after one stage of fractionation at 5000 rpm.

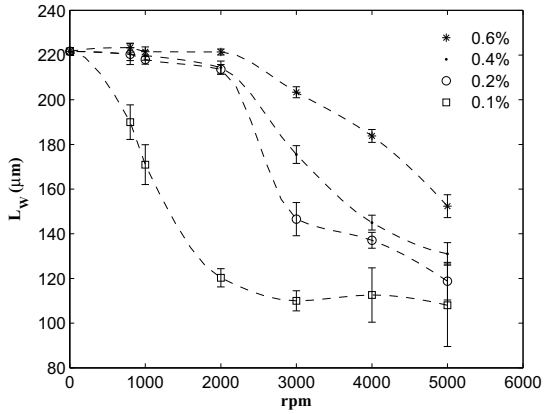

Figure 4.4: Effect of fibre consistency on length fractionation at different rotational velocities.

The effect of consistency is shown in Figure 4.4. Increasing fibre consistency results in a smaller reduction in fibril length. This might be due to the formation of fibre networks and increase in fibre-fibre interaction. If we normalize the fre-

quency of the fibrils remaining in each sample by their initial frequency and call it F_n, we can observe the reduction on yield efficiency as concentration is increased (Figure 4.5). Finally, to ensure that fractionation of the MFC samples had an effect on paper samples, we formed standard handsheets with additions of the MFC which was fractionated using the gel technique (retained fraction), see Figure 4.6. In both cases tensile index and strain at break of the fractionated MFC reinforced papers are enhanced over the papers reinforced with the original MFC. This can be contributed to the increase in the hydrogen bonds, more uniform distribution of stresses due to extended surface area of MFC and increase in fibre-fibre contact area. In fact we report a 25 % increase in the tensile index before fractionation and an additional increase of 10 % in tensile index and 120 % in strain at break after 10 % (wt/wt) of the fractionated MFC was added to the samples.

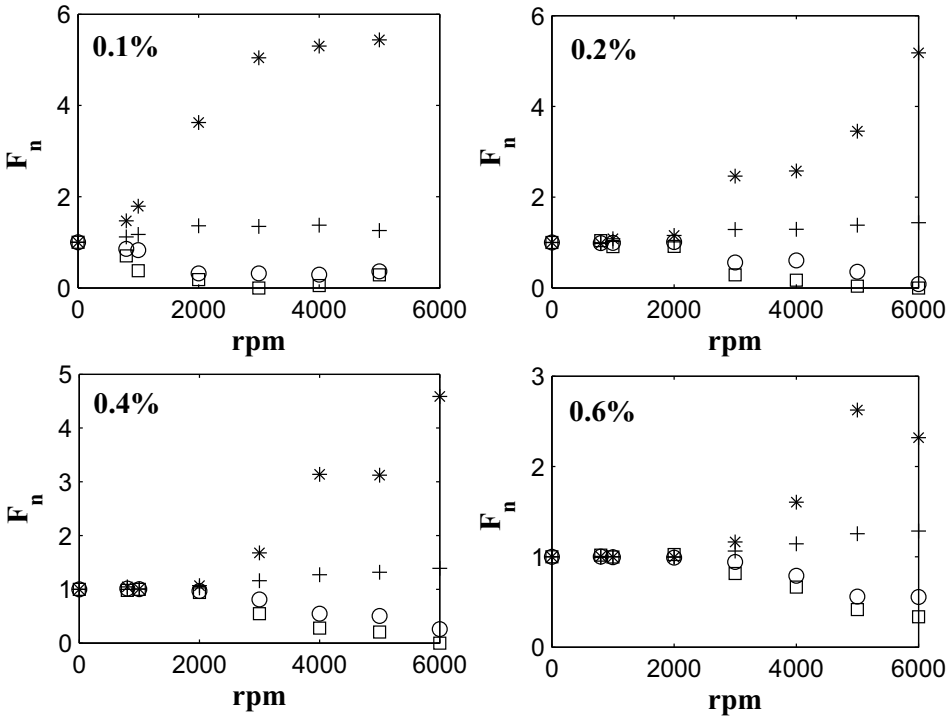

Figure 4.5: Variation of normalized fibril frequency Fn at different rotational velocities and fibril concentrations for retained sample. *, +, o and □ stand for 0-50 μm, 50-200 μm, 200-400 μm and 400-longer.

4.4 Summary and Conclusion

Three different fractionation techniques were tested to remove relatively long fibrils from an MFC samples. The results showed that all the three methods are capable of removing longer fractions of MFC. The gel fractionation technique shows a larger reduction in fibril length in comparison to either the hydrocyclone and pressure screen for the conditions tested. As shown in Figure 4.7 only one

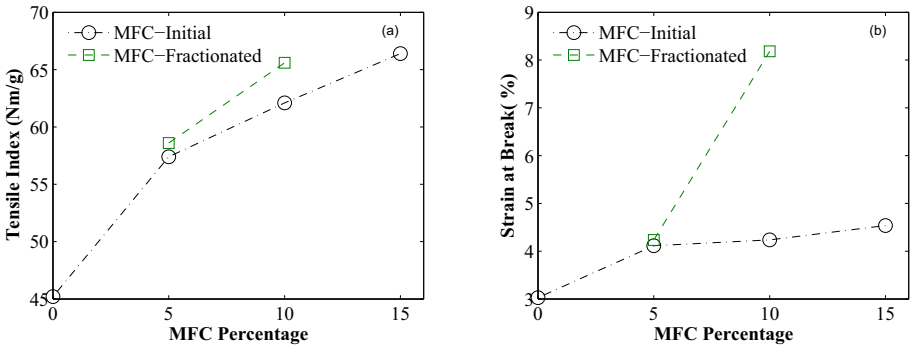

Figure 4.6: Changes in physical properties of MFC reinforced handsheets. In (a) tensile index increase and in (b) strain at break increase is shown before and after fractionated MFC is added to the handsheets.

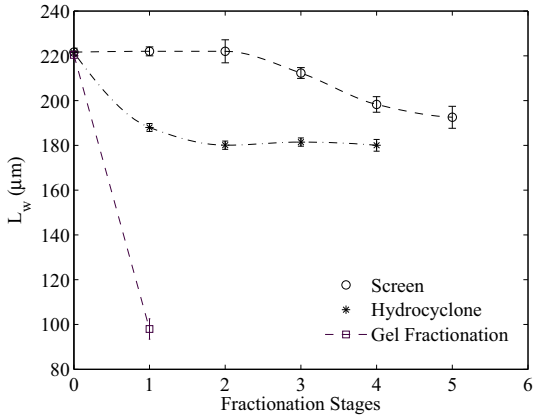

Figure 4.7: Comparison of three different fractionation techniques.

stage of fractionation using gel technique is more efficient than multiple stages of fractionation using slotted screen baskets and hydrocyclone, for the conditions tested. Results of strength tests showed improvement in the tensile index and strain at break of MFC-reinforced handsheets.

Chapter 5

Towards the Design of a Continuous Device

5.1 Introduction

In the previous chapters, it was found that separation can occur and indeed the process is quite efficient. The results however are based upon batchwise testing. If this methodology is to have any industrial significance, a continuous process must be developed.

To reiterate, the process which we have proposed involves particles being subjected to two different forces. The first force is the centrifugal force and this is the force which allows separation to occur. The second force, although not mentioned previously is the gravitational force. The gravitational force must be less than the yield stress (times area) otherwise the particle will settle before separating.

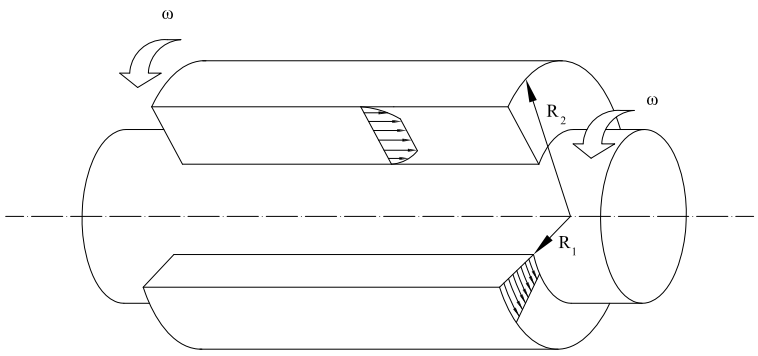

Figure 5.1: Schematic of the geometry considered.

For a continuous device, we need to consider a flow field in which the particles can translate in a direction orthogonal to the applied centrifugal force. In addition, the translational motion must be *independent* or decoupled from the motion induced by the centrifugal force. Finally, to achieve fractionation, fluid motion must occur in which a significant portion of the flow is in the unyielded stage.

The flow field considered to achieve these requirements is a pressure driven flow imposed onto solid body rotation. The flow field is highlighted in Figure 5.1, in which a pressure gradient derives a flow $\hat{W}(r)$ axially in the annular gap between two concentric cylinders. In addition to this, the walls of each cylinder rotate at the same angular rate and in the same direction. We define this flow as spiral Poiseuille flow.

This flow field allows particles to translate axially as well as migrate radially, if the applied centrifugal force is sufficient. As will be shown subsequently, as the axial and rotational flows are decoupled, the size of the plug or unyielded region in the centre of the channel, see Figure 5.2, can be controlled by the axial pressure drop alone. This would allow the user independent control of the separation and production rate.

The separation is envision to occur as follows:

1. The entire annular gap is filled with a viscoplastic gel that is slowly moving axially while rotating.

2. The axial velocity is set such that the size of the plug in the central portion of channel occupies a large fraction of the channel.

3. A particle rich suspension is introduced near the inner cylinder. The introduction of particles is limited to this region and does not extend over the entire radius of the inlet region.

4. The particles will translate with the flow. Some particles based on what outlined in the previous chapter will migrate to the outer periphery.

5. The device would have two exits to collect the sorted particle streams.

The questions which we are addressing in this chapter are: at what conditions is this flow field achievable and does the presence of the centrifugal force destabilize the flow and cause transition to turbulence? Here we consider the linear stability of this flow using a Bingham fluid as the constitutive model.

Determining the point of transition from laminar to turbulent flow for a viscoplastic fluid in this geometry is difficult, if not impossible. Insight into this can be gained by first considering the simpler problem of a pressure driven flow of a Newtonian fluid through a concentric annulus that is stationary, i.e. there is no swirl component. In perhaps one of the first studies in this area, Mott and Joseph (1968) demonstrate a unique feature of this flow. They show that in the limit of large annular gaps, i.e. in the limit of Hagen-Poiseuille, this flow is linearly stable. For all other cases, instability occurs and they report transition for unique combinations of axial flow rate, represented by a Reynolds number, and gap size.

When a swirling flow is imposed on this pressure driven axial flow, the point of transition is affected. Indeed, when two linearly stable flows are superimposed, in this particular example we refer to the case of when solid body rotation[1] is combined with Hagen-Poiseuille flow, Mackrodt (1976) demonstrates linear instability at a critical Reynolds number. Further examples of this destabilizing effect are found for cases of solid-body rotation in conjunction with either Poiseuille or Couette flows (Meseguer and Marques (2000), Meseguer and Marques (2002)).

For Bingham fluids, our understanding of transition with swirling, pressure-driven flows is somewhat less developed. These fluids are inelastic but have an effective viscosity that varies with the rate of strain. To clarify this latter relationship more clearly, if the deviatoric stress at any location in the fluid does not exceed a prescribed threshold, then the rate of strain is zero at that point; Unyielded regions behave effectively as rigid bodies undergoing linear and rotational

[1] Meseguer and Marques (2000) indicate that this class of flow is linearly stable.

motion. For steady, fully developed flows in annular gaps, solutions do exist in the literature for the fully-developed case, i.e. one-dimensional Poiseuille (Bird et al. (1983), Fordham et al. (1991)) and swirling Poiseuille flows (Bittleston and Hassager (1992), Liu and Zhu (2010)) with Bingham fluid models. These works indicate that under slow flow conditions an unyielded "plug" exists in the central portion of the gap with its size dictated by the ratio of the yield stress of the fluid to the applied pressure drop. For the case of swirling Poiseuille flows undergoing solid-body rotation, Bittleston and Hassager (1992) demonstrate that the axial flow field is not affected by the presence of the centrifugal force.

We now turn our attention to transition with Bingham fluids. A number of authors have studied transition for either the one dimensional Poiseuille flow case or for the purely swirling flow. For example, Frigaard et al. (1994) demonstrate that the margin for stability increases over that of a corresponding Newtonian fluid. Kabouya and Nouar (2003) advance the argument that a Poiseuille flow is always linearly stable to axisymmetric disturbances. Similarly, Landry et. al. (2006) show that solid body rotation of a Bingham fluid is always linearly stable. To the best of our knowledge, there are no works available in the literature studying the stability of spiral Poiseuille flows of Bingham fluids. We speculate, based upon the Newtonian results, that the superposition of these two linearly-stable flows may result in a case which is linearly unstable.

5.2 Basic Flow for Spiral Poiseuille Problem

The constitutive model that we consider throughout this chapter is that of a Bingham fluid. These are characterized by density $\hat{\rho}$, yield stress $\hat{\tau}_y$ and plastic viscosity $\hat{\mu}_p$. The geometry of the spiral Poiseuille flow is a channel formed in the annular gap between two concentric cylinders of radii $\hat{R}_1$ and $\hat{R}_2$ that rotate with the same angular speed $\hat{\omega}$. There is an imposed dimensional pressure gradient in the $\hat{z}$-direction $\hat{p} = -G\hat{z}$. Following Chossat and Iooss (1994), we nondimensionalize the Navier-Stokes equations using a length scale of $\hat{d} = \hat{R}_2 - \hat{R}_1$, a velocity $\hat{U}_0$ and time scale $\hat{t}_0$ of

$$\hat{U}_0 = \frac{\hat{d}^2 G}{2\hat{\mu}_p} \quad \hat{t}_0 = \frac{\hat{\rho}\hat{d}^2}{\hat{\mu}_p}$$

and a pressure-stress scale of $\hat{\mu}_p \hat{U}_0/\hat{d}$. Using these scalings, and omitting the hat notation for dimensionless variables, the scaled constitutive equations for the fluid are

$$\tau_{ij} = \left(1 + \frac{B}{\dot{\gamma}}\right)\dot{\gamma}_{ij} \iff \tau > B \tag{5.1}$$

$$\dot{\gamma} = 0 \iff \tau \leq B \tag{5.2}$$

where $\dot{\gamma}$ and τ are the rate of strain and stress tensors, respectively and B is Bingham number. These are defined by

$$\dot{\gamma} = \left[\frac{1}{2}\dot{\gamma}_{ij}\dot{\gamma}_{ij}\right]^{\frac{1}{2}}, \quad \tau = \left[\frac{1}{2}\tau_{ij}\tau_{ij}\right]^{\frac{1}{2}} \tag{5.3}$$

where $\dot{\gamma}_{ij} = u_{ij} + u_{ji}$. With these, we find that this flow is characterized by five dimensionless groups, the axial and tangential Reynolds numbers, Re_z and Re_θ, the Bingham number B, the ratio of the swirl and axial velocities, ω, and the ratio of the radii of the two cylinders, η:

$$Re_z = \frac{\hat{\rho}\hat{U}_0\hat{d}}{\hat{\mu}_p}, \quad Re_\theta = \frac{\hat{\rho}\hat{\omega}R_2\hat{d}}{\hat{\mu}_p}, \quad B = \frac{\hat{\tau}_y\hat{d}}{\hat{\mu}_p\hat{U}_0} \quad \omega = \frac{Re_\theta}{R_z R_2} \quad \eta = \frac{\hat{R}_1}{\hat{R}_2}. \tag{5.4}$$

If

$$r = \frac{\hat{r}}{\hat{d}} \qquad r \in [\frac{\eta}{1-\eta}, \frac{1}{1-\eta}] \tag{5.5}$$

the equations of motion reduce to

$$\mathbf{u}_t + Re_z(\mathbf{u}\cdot\nabla)\mathbf{u} = -\nabla p + \nabla\cdot\tau \tag{5.6}$$

$$\nabla\cdot\mathbf{u} = 0 \tag{5.7}$$

where $\mathbf{u}$ is the velocity, p the pressure and τ the deviatoric stress tensor.

Finally, a steady solution of the form

$$(P, \mathbf{U}(r,\theta,z)) = [P(r,z), 0, r\omega, W(r)]$$

exists where $W(r)$ may be determined using the methodology outlined by Liu and Zhu (2010). Here, a particular solution is derived from the general solution

$$\tau_{rz} = -r + \frac{c}{r} \tag{5.8}$$

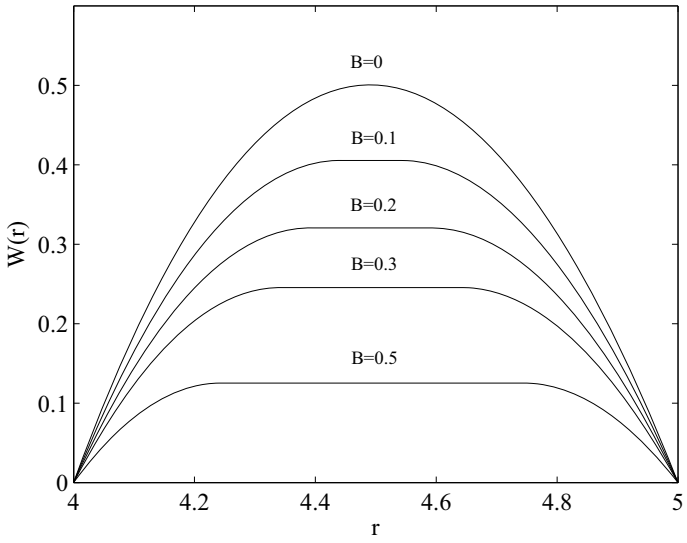

Figure 5.2: Representative examples of the axial velocity $W(r)$ for various Bingham numbers.

using the constitutive equation for a Bingham fluid as well as the no-slip conditions. Representative velocity profiles are given in Figure 5.2 as a function of B. The steady, fully-developed spiral Poiseuille flow consists of an unyielded region in the center of the channel, for finite B, bounded by two yielded regions. The position of the yield surfaces is found as part of the solution methodology in Liu and Zhu (2010) and is dependent only on B; the swirl component does not affect the position of the plug. The size of the plug H is calculated by applying the balance of shear forces and pressure forces on the boundaries of the plug zone and is given by $H = B$ (Liu and Zhu (2010)).

5.3 Linear Perturbation Equations

Here we consider the classical problem of linear stability, by perturbing the steady flow $(P, \mathbf{U})$, as described above, with an infinitesimally small disturbance on the flow field $(p', \mathbf{u}')$ and plug size h'. If

$$\mathbf{u} = \mathbf{U} + \varepsilon \mathbf{u}' \qquad p = P + \varepsilon p' \qquad h = H + \varepsilon h' \tag{5.9}$$

where $\varepsilon << 1$, we find that the equations of motion, i.e. Equations 5.6-5.7 reduce to

$$\begin{aligned} u'_t + Re_z(\frac{V}{r}\frac{\partial u'}{\partial \theta} + W\frac{\partial u'}{\partial z} - \frac{2V}{r}v') = -\frac{\partial p'}{\partial r} + \{\nabla^2 u' - \frac{2}{r^2}\frac{\partial v'}{\partial \theta} - \frac{u'}{r^2}\} + \\ B\{\frac{1}{r}\frac{\partial}{\partial r}(\frac{r\dot{\gamma}_{rr}}{\dot{\gamma}}) - \frac{\dot{\gamma}_{\theta\theta}}{r\dot{\gamma}} + \frac{1}{r}\frac{\partial}{\partial \theta}(\frac{\dot{\gamma}_{r\theta}}{\dot{\gamma}})\} \end{aligned} \tag{5.10}$$

$$\begin{aligned} v'_t + Re_z(u'\frac{\partial V}{\partial r} + \frac{Vu'}{r} + W\frac{\partial v'}{\partial z} + \frac{V}{r}\frac{\partial v'}{\partial \theta}) = -\frac{1}{r}\frac{\partial p'}{\partial \theta} + \\ \{\nabla^2 v' - \frac{v'}{r^2} + \frac{2}{r^2}\frac{\partial u'}{\partial \theta}\} + B\{\frac{\partial}{\partial z}(\frac{\dot{\gamma}_{\theta z}}{\dot{\gamma}}) + \frac{1}{r^2}\frac{\partial}{\partial r}(r^2\frac{\dot{\gamma}_{r\theta}}{\dot{\gamma}})\} \end{aligned} \tag{5.11}$$

$$\begin{aligned} w'_t + Re_z(u'\frac{\partial W}{\partial r} + \frac{V}{r}\frac{\partial w'}{\partial \theta} + W\frac{\partial w'}{\partial z}) = -\frac{\partial p'}{\partial z} + \{\nabla^2 w'\} + \\ B\{\frac{1}{r}\frac{\partial}{\partial \theta}(\frac{\dot{\gamma}_{z\theta}}{\dot{\gamma}}) + \frac{\partial}{\partial z}(\frac{\dot{\gamma}_{zz}}{\dot{\gamma}})\} \end{aligned} \tag{5.12}$$

when terms smaller than $O(\varepsilon^2)$ are eliminated. In the limit when $B = 0$, the disturbance equations reduce to that of the Newtonian case. For $B > 0$, as discussed previously, a plug exists in the central portion of the annulus.

To derive the eigenvalue problem we assume that the solution can be repre-

sented in terms of axi-symmetric normal modes of the form

$$(u', v', w', p', h') = (u(r), v(r), w(r), p(r), h) \exp(i\alpha z + \lambda t) \tag{5.13}$$

where α is the wave number and $\lambda = \lambda_r + i\lambda_i$ is the complex wave speed. Denoting

$$D \equiv \frac{d}{dr} \qquad L = D^2 + \frac{D}{r} - \frac{1}{r^2} - \alpha^2 \tag{5.14}$$

the linearized equations for the normal modes are found by substituting equation 5.13 into equation 5.10-5.12. After some algebraic manipulation the normal mode equations reduce to

$$-Re_z(uDV + \frac{uV}{r}) + Lv - WiRe_z\alpha v + B\phi_\theta = \lambda v \tag{5.15}$$

$$\begin{aligned} L^2u - Re_zW\alpha iLu + \alpha iRe_zD^2Wu - \alpha iDWRe_z\frac{u}{r} \\ - B\phi_r - \frac{2Re_zV\alpha^2}{r}v = \lambda Lu \end{aligned} \tag{5.16}$$

where

$$\phi_r = \frac{1}{r}\frac{\partial}{\partial r}(\frac{2rDu}{\dot{\gamma}}) - \frac{2u}{r^2\dot{\gamma}} \tag{5.17}$$

$$\phi_\theta = -\frac{\alpha^2 v}{\dot{\gamma}} + \frac{1}{r^2}\frac{\partial}{\partial r}(r^2\frac{\dot{\gamma}_{r\theta}}{\dot{\gamma}}) \tag{5.18}$$

If $\mathbf{x} = (u, v)$, these equations may be written as

$$\mathscr{A}\mathbf{x} = \lambda\mathscr{B}\mathbf{x} \tag{5.19}$$

where

$$\mathscr{A} = \mathscr{A}_V + Re_z\mathscr{A}_I + B\mathscr{A}_Y, \tag{5.20}$$

respectively denoting the viscous, inertial and yield stress parts of $\mathscr{A}$. These operators are defined by

$$\mathscr{A}_V = \begin{pmatrix} L^2 & 0 \\ 0 & L \end{pmatrix}, \qquad \mathscr{A}_I = \begin{pmatrix} \alpha i(D^2W - \dfrac{DW}{r} - WL) & -2\alpha^2\left(\dfrac{V}{r}\right) \\ -DV - \dfrac{V}{r} & -W\alpha i \end{pmatrix},$$

$$\mathscr{A}_Y = \begin{pmatrix} \phi_r & 0 \\ 0 & \phi_\theta \end{pmatrix}, \qquad \mathscr{B} = \begin{pmatrix} L & 0 \\ 0 & 1 \end{pmatrix},$$

The boundary conditions at the walls are

$$u = Du = v = 0 \tag{5.21}$$

and at the yield surfaces

$$u = Du = v = 0. \tag{5.22}$$

While the condition at Equation 5.21 is fairly obvious, the conditions at Equation 5.22 are not. The Dirichlet conditions come from consideration of the linear momentum of the plug region. The term Du is formed through the linearization of the condition $\dot{\gamma}_{ij}(\mathbf{U} + \mathbf{u}') = 0$ at the perturbed yield surface position onto the unperturbed yield surface position. Note that the problem defined above is posed

over the yield portion of the channel. The linear stability problem in the two yielded regions decouple to form two independent and equivalent problems. This observation was also reported by Kabouya and Nouar (2003).

We have solved the system of equation 5.19 using a Chebyshev discretization as described by Schmid and Henningson (2001). For fixed $(Re_z, Re_\theta, B, \eta, \alpha)$ we solve for the eigenvalues and eigenfunctions of equation 5.19, and take the eigenvalue with maximal real part, $\lambda_{R,max}(\alpha)$. At each $(Re_z, Re_\theta, B, \eta)$, an inner iteration calculates the wavenumber α_{max} for which $\lambda_{R,max}$ is largest. For the outer iteration, we vary Re_z until we find the point in which $\lambda_{r,max}(\alpha) = 0$. This root finding procedure was performed using MATLAB's built in function *fzero*, which is a combination of the bisection and interpolation methods.

To validate our code, we compare our work to that of Mott and Joseph (1968) and their results are compared with the case of $B = Re_\theta = 0$. Mott and Joseph (1968) studied the stability boundary of Poiseuille flow for a Newtonian fluid and reported the critical $Re_{z,cr}$ as a function of η. The results are shown in Figure 5.3. Our results are within 5% of those given by Mott and Joseph (1968). The convergence of the numerical method is shown in table-5.1, where the critical axial Reynolds numbers $Re_{z,cr}$ are presented as a function of the number of spectral modes (N) used for calculation in each case. It is important to note that this value changes for each aspect ratio η. Increasing η results in increase in the computational domain and as a result the number of spectral modes increases. Here for $\eta = 0.9$ the value of N was considered as $N = 125$.

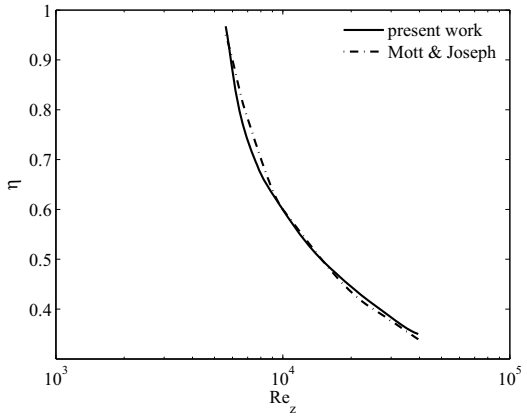

Figure 5.3: The margin of stability for Poiseuille flow of a Newtonian fluid. For this simulation $B = Re_\theta = 0$ and η as a parameter.

N	$Re_{z,cr}$
25	5.58018e+03
50	5.91056e+03
75	5.91062e+03
100	5.91062e+03
125	5.91062e+03

Table 5.1: Critical values of Re_z with increasing number N of Chebyshev polynomials. The case considered here was at $\eta = 0.9$, and $Re_\theta = B = 0$.

5.4 Results and Discussion

Before we proceed to the main findings of this chapter, we examine the Newtonian case in order to understand the effects of superposition of solid body rotation on a Poiseuille flow. This is shown in Figure 5.4-a, where we display representative values of $\lambda_{R,max}(\alpha)$ for a number of different Re_z. What is evident in this figure is that the largest value of $\lambda_{R,max}(\alpha)$ (a) increases with increasing Re_z and

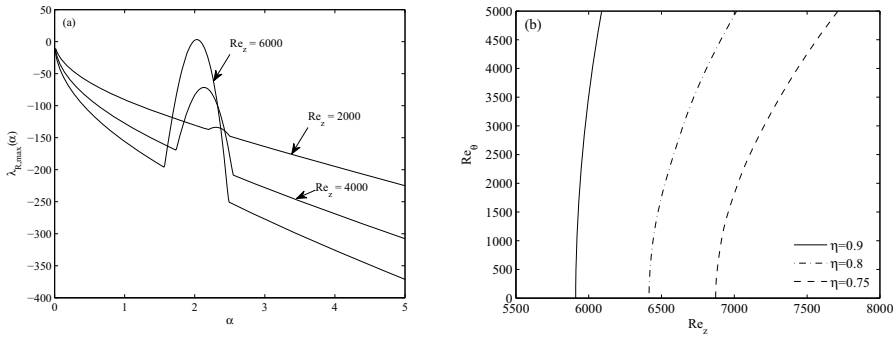

Figure 5.4: The linear stability of a Newtonian fluid $(B = 0)$ in spiral Poiseuille flow. In (a) we display $\lambda_{R,max}(\alpha)$ as a function of Re_z for a fixed annular gap of $\eta = 0.9$ and $Re_\theta = 0$. In (b), we display the margins of stability for the Newtonian case of the flow as a function of gap size.

(b) becomes positive somewhere in the region of $Re_z \in [4000, 6000]$. In Figure 5.4-b, a larger simulation was considered in which we determined the margin of stability at a number of representative η. What we see is that the slope of curve representing (Re_z, Re_θ) is positive, for all regions simulated, indicating that the centrifugal force has a stabilizing effect on this flow. In other words, at higher rotational rates, a larger critical Re_z is required to initiate instability. In addition, the Re_z generally increases with increasing gap sizes.

We now turn our attention to the main findings, that being the margin of stability for a Bingham fluid. We find that the flows are linearly stable over the same conditions tested for the Newtonian case. Specifically we find the flow stable over the region $[Re_z, Re_\theta, \eta] \in [0, 8000] \times [0, 5000] \times [0.75, 0.9]$. To highlight our findings, we show a typical results for $\lambda_{R,max}(\alpha)$ as a function of B in Figure 5.5. We find that $\lambda_{R,max}(\alpha)$ diminishes with increasing B and that the curves are mono-

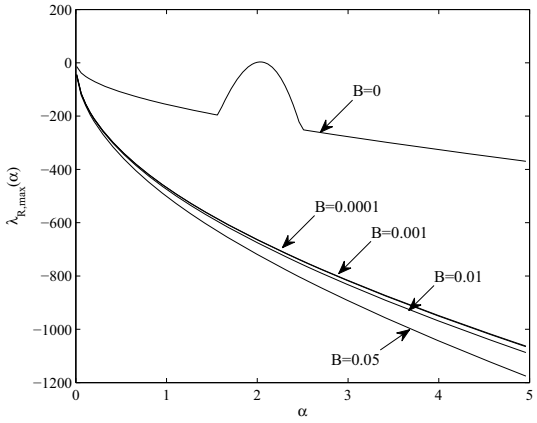

Figure 5.5: The linear stability of a Bingham fluid $(B > 0)$ in spiral Poiseuille flow. We display $\lambda_{R,max}(\alpha)$ as a function of B for a fixed annular gap of $\eta = 0.9$, $Re_\theta = 0$ and $Re_z = 6000$.

tonic over the range tested. We also find that this curve is always less than zero. These findings are similar to those presented by Kabouya and Nouar (2003) for Poiseuille flow of a Bingham fluid.

5.5 Summary

In this chapter we examine the linear stability of spiral Poiseuille flow of both Newtonian and Bingham fluids. Although this work was motivated from a fractionation application, the scientific goal was to examine the effect of the superposition of a linear stable flow onto a Poiseuille flow. We find that for the Newtonian case, instability did occur but the margin of stability did indeed increase with increasing Re_θ. For the Bingham fluid case, we find that the eigenvalue problem to be stable over the range $[Re_z, Re_\theta, \eta] \in [0, 8000] \times [0, 5000] \times [0.75, 0.9]$.

With regards to design of the continuous device, these findings demonstrate that solid body rotation stabilizes the flow of a Bingham fluid. This is encouraging as it will allow for greater production rates.

Chapter 6

Summary and Conclusions

In this work we advanced the argument of a novel separation principle. Here we propose that the separation principle is based upon controlling the threshold for motion of individual classes of particles. If the threshold can be controlled to a high enough resolution then in principle any separation could be achieved. In this work we set our threshold by the balance between the centrifugal force and the yield stress of a gel. Other systems could be used to control this to a finer scale.

This principle is strikingly different than that used in present industrial or even laboratory devices. The separation is related to parameters such as density, fluid properties, applied force and specific surface. The efficiency of this separation is diminished due to long-range hydrodynamic interactions.

We have demonstrated under very ideal conditions that separation can indeed be achieved with these types of gels. We found out that with rods the separation is based upon the mass per unit area of the particle and orientation has a large effect

on stability. It was shown that when the cylinders were oriented parallel to the direction of force, the threshold is independent of length for large L/D. Simple test cases were performed with nylon fibre suspensions in which separation was achieved based upon either length or diameter.

We argued that there are limitations to this proposed system before its reduction into practice. First, this system too is limited by the long range hydrodynamic interactions. However, the interactions are on a smaller scale and limited to the interaction length created by the unyielded envelope. In addition, we see that the separation is based upon the mass per unit area of the unyielded envelope. The size and shape of the envelope is still an open question in the literature. Understanding this will allow for an estimate of the upper limit of the efficiency of this proposed separation technique in terms of concentration and classes of particles which can be separated from each other.

Once the principle was demonstrated, we tested the utility of this method with two different papermaking suspensions. We found that indeed the methodology does work and was able to separate papermaking suspensions based upon length and coarseness, and MFC suspensions more efficiently than traditional techniques.

Finally, in the last portion of the work, we speculate the requirements to develop a continuous version of this principle. We found that a pressure driven flow superimposed upon to a swirling flow meets the requirements for separation. A demonstration of this however has yet to be conducted.

6.1 Future Work

The direction of the follow-up work in this line of work is quite clear. We have shown that a spiral Poiseuille flow has the potential to form a continuous device. The subsequent project should engage in developing this flow field and demonstrating the principle continuously.

Bibliography

ANDRES U.T. 1961 Equilibrium and motion of spheres in a viscoplastic liquid, *Sov. Phys. Doklady (U.S.A.)* **5**, 723–730.

ATTAPATU, D.D. CHHABRA R.P AND UHLHERR, J. 1995 Creeping sphere motion in Herschel-Bulkley fluids: flow field and drag, *J. Non-Newtonian Fluid Mech.* **59**, 245–265.

AZEREDO, H.M.C.D. 2009 Nanocomposites for food packaging applications, *Food Res. Int.* **42(9)**, 1240–1253.

AZIZI SAMIR,M.A.S., ALLOIN F. AND DUFRESNE,A. 2005 Review of recent research into cellulosic whiskers, their properties and their application in nanocomposite field, *Biomacromolecules* **5**, 612-626.

BATCHELOR, G.K. 1972 Sedimentation in a dilute dispersion of spheres, *J. Fluid Mech.* **123**, 245–268.

BEAULNE, M. AND MITSOULIS, E. 1997 Creeping motion of a sphere in tubes filled with Herschel-Bulkley fluids, *J. Non-Newtonian Fluid Mech.* **72**, 55–71.

BERGSTRÖM J. AND VOMHOFF H. 2007 Experimental hydrocyclone flow field studies, *Separation and Purification Technology* **53(1)**, 8–20.

BERIS, A.N. TSAMOPOULOS, J.A. ARMSTRONG, R.C. AND BROWN,R.A. 1985 Creeping motion of a sphere through a Bingham plastic, *J. Fluid Mech.* **158**, 219-244.

BYRON-BIRD, R., DAI, G.C. AND YARUSSO, B.J., 1983 The rheology and flow of visco-plastic materials, *Rev. Chem. Engng.* **1(1)**, 1–70.

BITTLESTON, S.H., AND HASSAGER, O., 1992 Flow of viscoplastic fluids in a rotating concentric annulus, *J. non-Newt. Fluid Mech.* **42**, 19–36.

BLACKERY, J. AND MITSOULIS, E. 1997 Creeping motion of a sphere in tubes filled with a Bingham plastic material, *J. Non-Newtonian Fluid Mech.* **70**, 59–77.

BLISS, T. 1984 Secondary fibre fractionation using centrifugal cleaners, *proceedings from the 1984 TAPPI Pulping Conference (Book2), Seattle* , 217–225.

BOYSAN, F. AYRES, W.H. AND SWITHENBANK, J. 1982 A fundamental mathematic modeling approach to cyclone design, *Trans IChemE* **60**, 222–230.

BUTLER, J.E. AND SHAQFEH, E.S.G 1989 Dynamic simulations of inhomogeneous sedimentation of rigid fibres, *J. Fluid Mech.* **468**, 205–237.

CHAPRA, S. 2006 Applied Numerical Methods with MATLAB for Engineers and Scientists, *second edition. McGraw-Hill* .

CHHABRA R.P. 2007 Bubbles, Drops and Particles in non-Newtonian fluids, (CRC, Boca Raton, Fl)

CHOSSAT, P. AND IOOSS, G. 1994 *The Couette-Taylor Problem,* Applied Mathematical Sciences series, volume 102, Springer-Verlag.

COPPICK, S., BROWN, R. 1963 Pulp processing method for mixed cellulosic materials, *Patent US 3301745* .

DUBIEF,D. SAMAIN E. AND DUFRESNE,A. 1999 Polysaccharide microcrystals reinforced amorphous poly(β-hydroxyoctanoate) nanocomposite materials, *Macromolecules* **32(18)**, 57655771.

DUFRESNE A., CAVAILLE J.Y. AND VIGNON M.R. 1997 Mechanical behavior of sheets prepared from sugar beet cellulose microfibrils, *J. App. Poly. Sci.* **64**, 1185–1194.

FENG, J. HU, H.H . AND JOSEPH, D.D. 1998 Direct simulation of initial value problems for the motion of solid bodies in a Newtonian fluid Part 1. Sedimentation, *J. Fluid Mech.* **261**, 95–134.

FORDHAM, E.J., BITTLESON, M.A., AND TEHRANI M.A. 1991 Viscoplastic flow in centered annuli, pipes and slots, *Ind. Engrg. Chem. Res* **39**, 517–524.

FORTIN, M. AND GLOWINISKI, R. 1983 Augmented Lagranian Methods (North Holland, Amsterdam)

FRIGAARD, I.A., HOWISON, S.D. AND SOBEY, I.J., 1994 On the stability of Poiseuille flow of a Bingham Fluid, *J. Fluid Mech.* **263**, 133–150.

FRIGAARD, I.A. AND NOUAR, C. 2005 On the usage of viscosity regularization methods for visco-plastic fluid flow computation, *J. Non-Newtonian Fluid Mech.* **127**, 1–26.

GLOWINISKI. R. AND LE TALLEK, P. 1987 Augmented Lagrangian and Operator Splitting Methods in Nonlinear Mechanics, *Studies in Applied and Numerical Mathematics* (Society for Industrial & Applied Mathematics, Philedelphia)

GUESLIN, B., TALINI, L., HERZHAFT, B., PEYSSON, Y. AND ALLAIN, C. 2006 Aggregation behavior of two spheres falling through an aging fluid, *Phys. Rev.* **74**, 042501.

HAJJI, P., CAVAILLE, J.Y., GAUTHIER C. AND VIGIER G. 1996 Tensile behavior of nanofibril and cellulose whiskers, *Poly. Comp.* **17(4)**, 612–619.

HAPPEL, J. AND BRENNER, H. 1965 Low Reynolds Number Hydrodynamics, *Prentice-Hall*.

HERZHAFT, B. AND GUAZZELLI, E. 1999 Experimental study of the sedimentation of dilute and semi-dilute suspensions of fibres, *J. Fluid Mech.* **384**, 133–158.

HOLM, R. STOREY, S. MARTINEZ, D.M AND SÖDERBERG, D. 2004 Visualization the motion of settling dilute rigid fibre suspensions, *Progress in Paper Physics* Trondheim Norway.

HSIEH, K.T. AND RAJAMANI, R.K. 1991 Mathematical model of the hydrocyclone based on physics of fluid flow, *AIChE J.* **37(5)**, 735–746.

HUBBE M. A., ROJAS O. J., LUCIA L. A., AND SAIN, M. 2008 Cellulosic nanocomposites: A review, *BioResources* **3(3)**, 929–980.

IWATAKE A., NOGI M., AND YANO M. 2008 Mechanical behavior of sheets prepared from sugar beet cellulose microfibrils, *Comp. Sci. Tech.* **68**, 2103-2106.

JAYAWEERA, K.O.L.F. AND MASON, B.J. 1965 The behavior of freely falling cylinders and cones in a viscous fluid, *J. Fluid Mech.* **22**, 709–720.

JIANZHONG, L., XING, S. AND ZHENJIANG, Y. 2003 Effects of the aspect ratio on the sedimentation of a fiber in Newtonian fluids, *J. Aer. Sci.* **34**, 909–921.

JIE, P. AND ZHU,K. Q. 2006 Drag force of interacting coaxial spheres in viscoplastic, *J. Non-Newtonian Fluid Mech.* **135**, 83–91.

JORDAN,J. JACOB,K.I., TANNENBAUM, R., SHARAF, M.A. AND JASIUK,I. 2005 Experimental trends in polymer nanocomposites: a review, *Mat. Sci. Eng.* **A(393)**, 1-11.

JOSSIC L. AND MAGNIN A 2001 Drag and stability of objects in a yield stress fluid, *AIChE J.* **47**, 2666-2672.

JULIEN SAINT AMAND, F., AND PERRIN, B. 1999 Fundamentals of screening: effect of rotor design and fibre properties, *Tappi Pulping Conf*, 941–945.

KABOUYA, N. AND NOUAR, C., 2003 On the stability of Bingham fluid flow in an annular channel, *C. R. Mecanique* **331**, 149–156.

KARLSSON, H. 1999 Improvements with L&W STFI Fibremaster, *PAPTAC Annual Meeting, Montreal, Canada* **90**, B1381–B1387.

KARNIS, A. 1997 Pulp fractionation by fibre characteristics, *Paperi ja Puu* **79(7)**, 480–488.

KEREKES, R.J., SOSZYNSKI, R.M. AND DOO, P.A.T. 1985 The flocculation of pulp fibres, *Eighth Fundamental Research Symposium* **Oxford**, 65-310

KO, J. 2005 Numerical Modeling of Highly Swirling flows in a cylindrical through flow hydrocyclone, *Licentiate Thesis* **KTH** Sweden

KOCH, D.L. AND SHAQFEH, E.S.G 1989 The instability of a dispersion of a dispersion of settling spheroids, *J. Fluid Mech.* **224**, 275–303.

KUMAR, P. AND RAMARAO, B.V. 1991 Enhancement of the sedimentation rates of fibrous suspensions, *Chem. Engng. Comm.* **108**, 381–401.

KURE, K., DAHLQVIST, G., EKSTROM, J. AND HELLE, T., 1999 Hydrocyclone separation, and reject refining, of thicked-wall mechanical pulp fibres, *Nordic Pulp Paper Res.* **14(2)**, 100–110.

LANDRY, M.P. FRIGAARD, I.A. AND MARTINEZ, D.M., 2006 Stability and instability of Taylor–Couette flows of a Bingham fluid, *J. Fluid. Mech.* **560**, 321-353.

LAPIERRE, L., BOUCHARD, J., AND BERRY, R. 1997 The relationship found between fibre length and viscosity of three different commercial kraft pulps, *Holzforschung* **63**, 402–407.

LAXTON, P.B. AND BERG J.C. 2005 Gel trapping of dense colloids, *J. Colloid Interface Sci* **285**, 152–157.

LI, M., JOHNSTON, R., XU, L., FILONENKO, Y. AND PERKER, I. 1999 Characterization of hydrocyclone-separated Eucalypt fibre fractions, *J. of Pulp and Paper Science* **25(8)**, 299–304.

LIU, Y.Q., ZHU, K.Q, 2010 Axial CouettePoiseuille flow of Bingham fluids through concentric annuli, *J. non-Newt. Fluid Mech.* **165**, 1494-1504.

LIU, B.T. MULLER, S.J. AND DENN, M. 2002 Convergence of a regularization method for creeping flow of a Bingham material around a rigid sphere, *J. Non-Newtonian Fluid Mech.* **102**, 179–191.

MA, L. INGHAM, D.B. AND WEN, X. 2000 Numerical modeling of the fluid and particle penetration through sampling cyclones, *J. Aer. Sci.* **31(9)**, 1097–1119.

MACKAPLOW, M.B. AND SHAQFEH, E.S.G 1998 A numerical study of the sedimentation of fibre suspensions, *J. Fluid Mech.* **376**, 149–182.

MACKRODT, P.A, 1976 Stability of Hagen-Poiseuille flow with superimposed rigid rotation, *J. Fluid. Mech.* **73**, 153–164.

MALM, G. E. 1967 Process of separating fibrous pulp into springwood and summerwood fibers by centrifuging, ,*Patent US3352745* .

MARTON, R. AND ROBIE, J.D. 1969 Characterization of mechanical pulps by a settling technique, *TAPPI J.* **22(12)**, 2400–2406.

MESEGUER, A. AND , MARQUES, F., 2000 On the competition between centrifugal and shear instability in spiral Couette flow, *J. Fluid. Mech.* **402**, 33–56.

MESEGUER, A. AND , MARQUES, F., 2002 On the competition between centrifugal and shear instability in spiral Poiseuille flow, *J. Fluid. Mech.* **455**, 129–148.

MOTT, J.E., AND JOSEPH, D.D. 1968 Stability of parallel flow between concentric cylinders, *Phys. Fluids* **11**(10), 2065–2073.

NAKAGAITO, A. N., A., SAKAI T. FUJIMURA, HAMA Y., AND YANO, H. 2009 Production of microfibrillated cellulosenext term (MFC)-reinforced polylactic acid (PLA) nanocomposites from sheets obtained by a papermaking-like process, *Composites Science and Technology* **69**, 1293–1297.

NARASHIMA, M. BRENNAN, M. AND HOLTHAM, P.N. 2007 Review of CFD modeling for performance prediction of hydrocyclones, *Engineering Applications of Computational Fluid Mechanics* **1(2)**, 109–125.

NOUAR, C., DEVIENNE, R AND LEBOUCHE, M. 1965 Convection thermique pour l'écoulement de Couette avec debit axial; cas d'un fluide pseudo-plastique, *Int. J. Heat. Mass Transfer* **30**(4), 639–647.

NOWAKOWSKI, A. F. AND DYAKOWSKI, T. 2003 Investigation of Swirling Flow Structure in Hydrocyclones, *Trans IChemE* **81(A)**, 862–874.

OLSON J.A., ROBERTS N., ALLISON B.J. AND GOODING, R.W 1999 Fibre length fractionation caused by pulp screening, *J. Pulp Paper Sci*, **24(12)**, 393–397.

PAAVILAINEN, L. 1992 The possibility of fractionating softwood sulfate pulp according to cell wall thickness, *Appita J.* **45(5)**, 319–326.

PARK, S., VENDITTI, H. JAMEEL, H. AND PAWLAK, J. J., 2005 The effect of fibre properties on fibre fractionation using a hydrocyclone, *J. of Pulp and Paper Science* **31 (3)**, 132–137.

PAAVILAINEN, L. 1992 The possibility of fractionating softwood sulfate pulp according to cell wall thickness, *Appita J.* **45(5)**, 319–326.

PENG, J. AND ZHU, K.-Q., 2004 Linear stability of Bingham fluids in spiral Couette flow, *J. Fluid Mech.* **512**, 21–45.

PUTZ, A. BURGHELEA, T. FRIGAARD, I.A. AND MARTINEZ, D.M. 2008 Settling of an isolated spherical particle in a yield stress fluid, *Phys. Fluids* **20(3)**, 033102–033102,11.

RICHARDSON J.F. AND ZAKI W.N. 1954 Sedimentation and fluidization, Part 1, *Trans. Instn Chem. Engrs.* **(32)**, 35–53.

RICKER, N. L. AND HOUSE, K.L. 1984 Thickening of pulp suspension in a hydrocyclone, *AIChE Symposium Series* **80(232)**, 8–16.

ROQUET, N. AND SARAMITO, P. 1983 An adaptive finite element method for Bingham fluid flows around a cylinder, *Comput. Methods Appl. Mech. Eng.* **192**, 3317–3341.

SALMELA, J. MARTINEZ, D.M. AND KATAJA, M. 2007 Sedimentation of dilute and semi-dilute rigid fibre suspensions at finite Re, *AIChE J.* **53(8)**, 1916–1923.

SCHMID, P.J. AND HENNINGSON, D.S., 2001 *Stability and transition in shear flows*, Springer-Verlag.

SEVILLA, E.M. AND BRANION, R.M.R. 1997 The Fluid dynamics of hydrocyclones, *J. Pulp Pap. Sci.* **23(2)**, 85–93.

SLOANE, C.M. 2000 Kraft pulp processing - pressure screen fractionation, *Appita J.* **53(3)**, 220–226.

TABUTEAU, H. COUSSOT, P. AND DE BRUYN, J.R. 2007 Drag force on a sphere in steady motion through a yield stress fluid, *J. Rheol.* **51**, 125–137.

TURBAK A. F., SNYDER F. W., SANDBERG K. R. 1983 Microfibrillated cellulose, a new cellulose product: Properties, uses, and commercial potential, *J. Appl. Polym. Sci., Appl. Polym. Symp.* , 815–827.

VOMHOFF H. AND GRUNDSTRÖM, K.J. 2003 Fractionation of a bleached softwood pulp and separate refining of the earlywood and latewood enriched fractionation, *Das Papier* **2**, 37.

WOOD, J. R. AND KARNIS, A. 1977 Towards a lint-free newsprint sheet, *Paperi ja Puu* **10**, 660–674.

WOOD, J. R. AND KARNIS, A. 1979 Distribution of fibre specific surface of papermaking pulps, *Pulp and Paper Canada* **80 (4)**, 73–78.

Appendix A

Experimental Details

In chapter 2 we measure the critical force required to initiate motion of a particle in a yield stress fluid under the action of a centrifugal force. Two different centrifuges were used depending upon the force required. For low rotational speed experiments an in-house centrifuge was built. In this case, the centrifuge, which was made from Plexiglas, was 250 cm in diameter, and 5 cm thick and was driven by a motor and controller, with a precision of 5 rpm, up to a maximum of rotational rate of 300 rpm. High speed experiments were conducted in a Universal Model UV centrifuge at rotational rates of up to 3000 rpm. The main fluid used in this study was Carbopol-940 obtained from Noveon. In most of the work a 0.16% (wt/wt) solution was prepared using DI water and then neutralized using a dilute *NaOH* solution. The density of the resulting solution was that of water. The resulting gels were degassed and then allowed to rest overnight.

Rheological characterizations were performed at room temperature in a cone and plate flow geometry on a Bohlin rheometer. Shear sweeps were performed in controlled strain mode typically in the range of $1 \times 10^{-2}\,\mathrm{s}^{-1}$ to $1\,\mathrm{s}^{-1}$ in order to determine the yield stress.

D (mm)	τ_y (Pa)	N	F_c
2.4	0.9	70	$29(\pm 0.7)$
2.4	3.1	200	$24(\pm 1)$
3.2	0.9	150	$23(\pm 1.3)$
3.2	3.3	150	$20.3(\pm 0.4)$
4.0	3.1	75	$17.4(\pm 0.3)$
4.0	3.3	170	$17.3(\pm 0.3)$
4.8	3.1	150	$14.8(\pm 0.3)$
4.8	3.3	170	$14.4(\pm 0.2)$
5.6	3.1	70	$13.6(\pm 0.5)$
5.6	3.3	130	$13.2(\pm 0.3)$

Table A.1: The experimental conditions for determination of F_c for spherical particles. The spheres in this case all had a density of 7800 kg/m^3. N represents the number of replicates and the uncertainty in F_c is reported at the 95% confidence interval.

τ_y (Pa)	ρ (kg/m^3)	D (mm)	L/D	N	F_c
3.3	7800	1.6	6.0	90	190($\pm$3)
3.3	7800	1.6	12.0	50	372($\pm$9)
3.3	7800	1.6	16.0	55	517($\pm$17)
3.3	7800	2.4	2.6	110	83($\pm$1)
3.3	7800	1.6	4.0	100	127($\pm$2)
3.3	7800	3.2	2.0	90	50($\pm$1)
3.3	7800	3.2	3.0	120	90($\pm$2)
3.3	7800	3.2	4.0	95	118($\pm$3)
4.0	8300	1.6	4.0	80	115($\pm$2)
4.0	8300	1.6	6.0	75	179($\pm$4)
4.0	8300	1.6	8.0	75	237($\pm$5)
4.0	8300	3.2	3.0	60	81($\pm$2)
4.0	8300	3.2	4.0	75	124($\pm$3)
4.0	8300	3.2	5.0	75	145($\pm$4)
4.0	8300	3.2	6.0	90	174($\pm$5)
4.0	8300	4.8	2.6	85	77($\pm$2)
4.0	8300	4.8	3.3	65	107($\pm$3)
4.0	8300	4.8	4.0	70	114($\pm$4)

Table A.2: The experimental conditions for determination of F_c for cylindrical rods with their axes oriented normal to the direction of force. N represents the number of replicates and the uncertainty in F_c is reported at the 95% confidence interval.

τ_y (Pa)	ρ (kg/m^3)	D (mm)	L/D	N	F_c
4.0	2700	1.6	16.0	50	183($\pm$5)
4.0	2700	1.6	20.0	50	169($\pm$6)
4.0	2700	1.6	28.0	30	214($\pm$5)
4.0	7800	1.6	4.0	85	49($\pm$2)
4.0	7800	1.6	6.0	75	59($\pm$2)
4.0	7800	1.6	8.0	80	67($\pm$3)
4.0	7800	1.6	12.0	90	96($\pm$3)
4.0	7800	1.6	16.0	70	128($\pm$6)
4.0	7800	1.6	20.0	90	170($\pm$12)
4.0	7800	1.6	25.0	55	165($\pm$7)
4.0	7800	2.4	2.6	70	37($\pm$1)
4.0	7800	2.4	4.0	80	52($\pm$2)
4.0	7800	2.4	6.6	95	80($\pm$3)
4.0	7800	2.4	8.0	95	111($\pm$4)
4.0	7800	2.4	10.6	65	115($\pm$2)
4.0	7800	3.2	2.0	100	28($\pm$1)
4.0	7800	3.2	3.0	120	43($\pm$2)
4.0	7800	3.2	4.0	100	51($\pm$3)
4.0	7800	3.2	6.0	80	79($\pm$3)
4.0	7800	3.2	8.0	65	103($\pm$4)
4.0	7800	4.8	2.0	80	33($\pm$1)
4.0	7800	4.8	2.6	80	41($\pm$2)
4.0	7800	4.8	3.3	70	51($\pm$2)
4.0	7800	4.8	4.0	65	57($\pm$2)
4.0	8300	1.6	4.0	90	60($\pm$2)
4.0	8300	1.6	6.0	100	83($\pm$2)
4.0	8300	1.6	8.0	100	114($\pm$3)
4.0	8300	3.2	3.0	80	47($\pm$1)
4.0	8300	3.2	4.0	80	66($\pm$2)
4.0	8300	3.2	5.0	100	70($\pm$2)
4.0	8300	3.2	6.0	90	75($\pm$4)
4.0	8300	4.8	2.6	90	45($\pm$2)
4.0	8300	4.8	3.3	80	65($\pm$2)
4.0	8300	4.8	4.0	75	75($\pm$2)

Table A.3: The experimental conditions for determination of F_c for cylindrical rods with their axes oriented parallel to the direction of force. N represents the number of replicates and the uncertainty in F_c is reported at the 95% confidence interval.

L/D	S/L	N	F_c
10	0.51	20	183($\pm$8)
10	0.70	20	183($\pm$14)
10	0.89	20	233($\pm$14)
16	0.59	30	244($\pm$37)
16	0.71	30	290($\pm$17)
16	0.83	30	319($\pm$12)
20	0.50	60	267($\pm$12)
20	0.63	60	363($\pm$14)
20	0.82	60	423($\pm$23)

Table A.4: The experimental conditions for determination of F_c for bent cylindrical rods with their axes oriented normal to the direction of force, see Figure 2.5. In this case the density of the fibres were 7800 kg/m^3, $\tau_y = 5.3$ Pa, and $D = 1.6$ mm. N represents the number of replicates and the uncertainty in F_c is reported at the 95% confidence interval.

L/D	S/L	N	F_c
10	0.51	60	139($\pm$5)
10	0.63	60	117($\pm$4)
10	0.82	60	87($\pm$4)
16	0.59	50	213($\pm$5)
16	0.71	50	190($\pm$6)
16	0.83	50	129($\pm$4)
20	0.57	50	247($\pm$5)
20	0.07	55	238($\pm$6)
20	0.89	40	220($\pm$5)

Table A.5: The experimental conditions for determination of F_c for bent cylindrical rods with their axes oriented parallel to the direction of force, see Figure 2.5. In this case the density of the fibres were 7800 kg/m^3, $\tau_y = 5.3$ Pa, and $D = 1.6$ mm. N represents the number of replicates and the uncertainty in F_c is reported at the 95% confidence interval.

Appendix B

Separation of Papermaking Fibres

In chapter 3 we measured the angular velocity required to initiate motion of a papermaking fibre suspension in a yield stress fluid under the action of a centrifugal force. The centrifuge used was a Universal Model UV centrifuge at rotational rates of up to 3500 rpm. 50 ml plastic tubes with 3 cm diameter were used as the fluid containers inside the centrifuge. The moment arm of the centrifuge was 15 cm. The main fluid used in this study was Carbopol-940 obtained from Noveon. In this work a 0.16 % (wt/wt) Carbopol solution was prepared using DI water and then neutralized using a dilute NaOH solution. The density of the resulting solution was that of water. The resulting gels were degassed and then allowed to rest overnight. Rheological characterizations were performed at room temperature in a cone and plate flow geometry on a Bohlin rheometer. Shear sweeps were performed in controlled strain mode typically in the range of 1 10^{-2} s^{-1} to 1s^{-1} in order to determine the yield stress. A number of different studies were performed

in which time, consistency, and initial fibre aspect ratio distributions were varied. The pulp in use was a semi-bleached kraft pulp (80 % Pine and 20 % Spruce-Fir).

Fibre Length(mm)	Fibre Diameter (μm)	Standard Deviation
0.5	23.70	0.55
1.5	28.76	0.58
2.5	30.69	0.52
3.5	31.20	0.64
4.5	31.37	1.45

Table B.1: A proposed relationship between length and diameter after averaging of semi-bleached kraft pulp used in the experiments.

Sample (j)	Screen Size	Ave. Fibre Length L_j (mm)	Ave. Coarseness (mg/m)
1	unfractionated	2.401($\pm$0.018)	0.113($\pm$0.003)
2	Mesh 14	3.631($\pm$0.200)	0.188($\pm$0.023)
3	Mesh 28	2.972($\pm$0.173)	0.132($\pm$0.014)
4	Mesh 48	2.028($\pm$0.059)	0.125($\pm$0.021)
5	Mesh 100	1.539($\pm$0.017)	0.086($\pm$0.005)
6	Mesh 200	0.617($\pm$0.003)	0.081($\pm$0.002)

Table B.2: The length-weighted mean fibre length and coarseness of samples in Figure 3.3. The errors represent standard deviation.

Fibre Class (i)	Fibre Length (L_i) (mm)	Range (mm)	Coarseness (mg/m)
1	0.75	$0-1.5$	0.096
2	2.25	$1.5-3$	0.130
3	3.75	$3-4.5$	0.172
4	5.25	$4.5-6$	0.225

Table B.3: The bin sizes and average values of coarsenesses of each bin. The errors represent standard deviation.

Average Fibre Length(mm)	Time ($minutes$)	Standard Deviation
2.25	0	0.02
1.85	2	0.02
1.57	6	0.10
1.36	10	0.04
1.01	14	0.01
1.00	18	0.13
0.95	22	0.01
0.97	30	0.05

Table B.4: The change in average fibre length of the retained fibres as the duration of applying the force is increased.

rpm	0-1 (mm)	1-2 (mm)	2-3 (mm)	3-4 (mm)
0	0.04	0.12	0.31	0.50
1100	0.05	0.14	0.31	0.48
1500	0.09	0.20	0.31	0.38
1900	0.16	0.25	0.31	0.27
2400	0.26	0.20	0.26	0.16
2800	0.43	0.28	0.16	0.11

Table B.5: Variation of fibre mass fraction in each bin as rpm is increased as shown in figure 3.7.

rpm	0-1 (mm)	1-2 (mm)	2-3 (mm)	3-4 (mm)
0	0.032	0.140	0.327	0.499
800	0.037	0.141	0.313	0.507
1400	0.038	0.144	0.347	0.468
1800	0.033	0.137	0.342	0.485
2200	0.046	0.166	0.334	0.452
2600	0.074	0.227	0.334	0.362
2900	0.247	0.262	0.228	0.261

Table B.6: Normalized mass fraction at 0.01% consistency as rpm is varied as shown in figure 3.8-a.

rpm	0-1 (mm)	1-2 (mm)	2-3 (mm)	3-4 (mm)
0	0.041	0.132	0.327	0.498
800	0.048	0.148	0.316	0.486
1400	0.045	0.138	0.333	0.482
1800	0.054	0.142	0.335	0.467
2200	0.090	0.210	0.329	0.370
2600	0.163	0.259	0.309	0.266
2900	0.296	0.254	0.26	0.187

Table B.7: Normalized mass fraction at 0.07% consistency as rpm is varied as shown in figure 3.8-b.

rpm	0-1 (mm)	1-2 (mm)	2-3 (mm)	3-4 (mm)
0	0.055	0.135	0.309	0.500
800	0.053	0.133	0.304	0.509
1400	0.060	0.144	0.319	0.474
1800	0.052	0.134	0.317	0.495
2200	0.093	0.175	0.297	0.432
2600	0.152	0.232	0.279	0.335
2900	0.230	0.269	0.285	0.213

Table B.8: Normalized mass fraction at 0.28% consistency as rpm is varied as shown in figure 3.8-c.

rpm	0-1 (mm)	1-2 (mm)	2-3 (mm)	3-4 (mm)
0	0.054	0.130	0.295	0.519
800	0.054	0.133	0.301	0.509
1400	0.056	0.127	0.305	0.510
1800	0.077	0.164	0.317	0.440
2200	0.09	0.249	0.289	0.371
2600	0.152	0.236	0.287	0.326
2900	0.308	0.263	0.251	0.176

Table B.9: Normalized mass fraction at 0.56% consistency as rpm is varied as shown in figure 3.8-d.

rpm	Bottom (mg/m)	Top (mg/m)	Weight Ratio
0	0.151 ($\pm$0.015)	0.151 ($\pm$0.018)	0.30
600	0.155 ($\pm$0.014)	0.144 ($\pm$0.011)	0.31
800	0.158 ($\pm$0.025)	0.138 ($\pm$0.006)	0.42
1000	0.164 ($\pm$0.006)	0.135 ($\pm$0.012)	0.74
1200	0.144 ($\pm$0.008)	0.125 ($\pm$0.013)	0.89
1400	0.162 ($\pm$0.015)	0.127 ($\pm$0.009)	0.92
1600	0.151 ($\pm$0.016)	0.124 ($\pm$0.006)	0.96

Table B.10: Fractionation results of mesh-14 fraction based upon coarseness at 0.05% fibre consistency as shown in figure 3.9.

Appendix C

Separation of MFC

Microfibrillated cellulose (MFC) samples, obtained from JRS (www.jrs.de), were used in chapter 4 (with the commercial name of NFC). The samples had an average fibre length of 221 μm as determined using an L & W STFI Fibremaster.

In the first technique, the MFC was fractionated using four hydrocyclone stages. Here we employed a C-1201 Y Microspin polypropylene hydrocyclone (www.natcogroup.com) with 10mm diameter and operated at 5 bar at a feed flow rate of 4.2 lpm; the initial consistency was set at 0.2 % and accept to reject ratio was set to 6 to 4.

In the second technique we employed a Metso FS-03 pressure screen to fractionate the initial MFC sample. Here, we collected the accept and progressively fractionated the sample by passing it through screens with progressively smaller slot sizes, namely 0.13, 0.09 and 0.06 mm. The screen was operated with five different initial concentrations, which were 0.1 %, 0.3 %, 0.5 %, 0.6 % and 1 %,

with a foil type rotor rotating at 3500 rpm and at a reject ratio of 60 %. After each step the collected samples were diluted to reach the minimum required volume of 15 L.

The last set of fractionation experiments was based on controlling the criteria of motion of particle suspended in a weak gel during centrifugation. Here an Eppendorf 5804 centrifuge was used with six 50 mL cylindrical containers and the rotational velocity up to 5000 rpm. In the experiments a 0.16 % (wt/wt) Carbopol solution (Noveon) was dissolved gently in DI (deionized) water and then neutralized using NaOH solution. The resulting fluid was a clear fluid with density of water and a yield stress of approximately 1 Pa. The MFC suspension was then mixed into the Carbopol solution and subjected to a prescribed rotational rate; four different initial concentrations were tested, i.e. 0.1 %, 0.2 %, 0.4 %, and 0.6 % (wt MFC/wt suspension). The top two third of the samples in each test tube were collected as fractionated MFC.

Finally, the fractionated MFC (the retained fraction) was mixed into a chemical pulp (bleached hardwood) at 4 different mass fractions (0, 5, 10 and 15 %). Standard handsheets (Scandinavian SCAN-C standard) were then formed using both initial and fractionated MFC and the tensile strengths of the paper samples were evaluated.

Stage	Pressure Screen (μm)	Hydrocyclone (μm)
Initial	221.6 ($\pm$1.8)	221.6 ($\pm$1.8)
1	219.0 ($\pm$2.2)	187.9 ($\pm$1.79)
2	220.2 ($\pm$3.2)	180.0 ($\pm$1.84)
3	207.5 ($\pm$1.8)	181.0 ($\pm$1.86)
4	199.4 ($\pm$2.6)	180.0 ($\pm$2.61)
5	190.0 ($\pm$2.4)	

Table C.1: Fractionation results of multi-stage fractionation using pressure screen and hydrocyclone.

rpm	0.6%	0.4%	0.2 %	0.1%
0	221.6 ($\pm$1.8)	221.6 ($\pm$1.8)	221.6 ($\pm$1.8)	221.6 ($\pm$1.8)
800	222.0 ($\pm$2.0)	220.4 ($\pm$4.7)	220.4 ($\pm$2.9)	190.0 ($\pm$7.7)
1000	221.5 ($\pm$2.2)	219.8 ($\pm$2.1)	218.0 ($\pm$2.1)	170.9 ($\pm$8.9)
2000	221.4 ($\pm$1.3)	214.5 ($\pm$2.9)	213.6 ($\pm$2.1)	120.3 ($\pm$4.1)
3000	203.4 ($\pm$2.4)	174.0 ($\pm$4.0)	146.5 ($\pm$7.4)	110.0 ($\pm$4.5)
4000	183.8 ($\pm$2.9)	145.0 ($\pm$3.3)	137.1 ($\pm$3.6)	112.6 ($\pm$12.2)
5000	152.4 ($\pm$5.1)	131.0 ($\pm$5.0)	118.8 ($\pm$8.4)	108.0 ($\pm$18.5)

Table C.2: Average fibre length(μm) of fractionation results of MFC using gel technique and effect of fibre consistency as shown in figure 4.4.

rpm	0-0.05 (mm)	0.05-0.2 (mm)	0.2-0.4 (mm)	0.4-0.8 (mm)	0.8-1.2 (mm)	1.2 (mm)
0	1.0	1.0	1.0	1.0	1.0	1.0
800	1.5	1.1	0.9	0.7	0.3	0.6
1000	1.8	1.2	0.8	0.4	0.3	0.0
2000	3.6	1.4	0.3	0.2	0.0	0.0
3000	5.0	1.3	0.3	0.0	0.0	0.0
4000	5.3	1.4	0.3	0.1	0.0	0.0
5000	5.4	1.3	0.4	0.3	0.0	0.0

Table C.3: Values of normalized mass fraction at 0.1% consistency as centrifugal force is increased as shown in figure 4.5-a.

rpm	0-0.05 (mm)	0.05-0.2 (mm)	0.2-0.4 (mm)	0.4-0.8 (mm)	0.8-1.2 (mm)	1.2 (mm)
0	1.0	1.0	1.0	1.0	1.0	1.0
800	1.0	1.0	1.0	1.0	0.7	3.2
1000	1.0	1.0	1.0	0.9	0.8	0.5
2000	1.2	1.0	1.0	0.9	0.6	0.6
3000	2.5	1.3	0.6	0.3	0.0	0.0
4000	2.6	1.3	0.6	0.2	0.0	0.0
5000	3.5	1.4	0.4	0.0	0.0	0.0

Table C.4: Values of normalized mass fraction at 0.2% consistency as centrifugal force is increased as shown in figure 4.5-b.

rpm	0-0.05 (mm)	0.05-0.2 (mm)	0.2-0.4 (mm)	0.4-0.8 (mm)	0.8-1.2 (mm)	1.2 (mm)
0	1.0	1.0	1.0	1.0	1.0	1.0
800	1.0	1.0	1.0	1.0	1.0	0.7
1000	1.0	1.0	1.0	1.0	0.9	0.8
2000	1.1	1.0	1.0	0.9	0.9	0.6
3000	1.7	1.2	0.8	0.5	0.3	0.3
4000	3.1	1.3	0.5	0.3	0.0	0.0
5000	3.1	1.3	0.5	0.2	0.0	0.0

Table C.5: Values of normalized mass fraction at 0.4% consistency as centrifugal force is increased as shown in figure 4.5-c.

rpm	0-0.05 (mm)	0.05-0.2 (mm)	0.2-0.4 (mm)	0.4-0.8 (mm)	0.8-1.2 (mm)	1.2 (mm)
0	1.0	1.0	1.0	1.0	1.0	1.0
800	1.0	1.0	1.0	1.0	1.1	0.8
1000	1.0	1.0	1.0	1.0	1.1	0.6
2000	1.0	1.0	1.0	1.0	0.9	0.6
3000	1.2	1.1	0.9	0.8	0.6	0.2
4000	1.6	1.1	0.8	0.7	0.4	0.3
5000	2.6	1.3	0.6	0.4	0.0	0.0

Table C.6: Values of normalized mass fraction at 0.6% consistency as centrifugal force is increased as shown in figure 4.5-d.

	no MFC	5% MFC	10% MFC	15% MFC	5% MFC Fractionated	10% MFC Fractionated
Tensile Index (Nm/g)	45.2	57.4	62.1	66.4	58.6	65.6
Strain at Break $(\%)$	3	4.1	4.2	4.5	4.2	8.2

Table C.7: Changes in physical properties of MFC reinforced handsheets as shown in figure 4.6.

Appendix D

Matlab Codes

In this appendix, the Matlab codes used to study stability analysis are presented. The main code is “stabilitiBoundary.m” which is followed by the sub functions.

```
%This code results in the stability boundary eta-Re
%for Newtonian flow in an
%annular region and reproduces the results of
% Mott & Josef. For aspect
%ratios eta<0.35
clear
clc
i=1;B=0.0001;N=25;
Re1=2*10^4;Re2=0;
for eta=0.9
%     [W,DW,DDW,r]=Daxial2_Low(B,eta,N);
    [Re_zero]=Re_lambda(eta,Re1,Re2,N,B);
    Re(i)=Re_zero;
    Eta(i)=eta;
    i=i+1;
end
B=(1-Eta.^2)./(2*log(1./Eta));
A=1-B.*(1-log(B));
Vratio=A./(2*(1-Eta).^2);
Re=Re*Vratio;
hold on
plot(Re,Re2,'ok')
xlabel('Re')
ylabel('Re2')
ylim([0 Re2+1000])
% characteristic length is d=R2-R1.
%The caracteristic velocity is chosen as U0=G*d^2/(4*mu)
%in order to produce Mott & Josef results, the Reynolds
% had to be converted as explained in the notes. Mott
%and Josef had chosen the characteristic velocity as
%the maximum velocity in the annulus while I had chosen
%the maximum velocity in the pipe. Their characteristic
%length was (R2-R1)/2 and min was (R2-R1). Therefore the
% Re obtained from my calculations had to
%be multiplied by Vratio to gain the correct result.
```

```
function [x]=axial2(eta,B)
%This Programs solves the axial Poiseuille flow of
 Bingham
%Fluids. it uses
% the method explained in "Axial CouettePoiseuille
flow of
% Bingham fluids
% through concentric annuli" J.N.N.F.M 2010[Liu & zhu]
 but the
% characteristic length is d=R2-R1.
%The caracteristic velocity is chosen as U0=G*d^2/(4*mu)
R1=eta/(1-eta);%inner radious in meter
R2=1/(1-eta);%outer radious in meter
% Bingham=-2tau0/(d*G)
i=1;
%x(1)=C1, x(2)= C2, x(3)=C3, x(4)=C4,
%x(5)=r1, x(6)=r2, x(7)=Uplug
x0 = [1;1;1;1;1;1;0.5]; % Make a starting guess at
the solution
[x,fval] = fsolve(@axialV,x0,[],B,R1,R2);
for r = R1: 0.01 : R2
    if r < x(5)
        w(i)=-1*r^2+x(1)*log(r)-B*r+x(2);
    end
    if r <x(6) && r > x(5)
        w(i)=x(7);
    end
    if r > x(6)
        w(i)=-1*r^2+x(3)*log(r)+B*r+x(4);
    end
    R(i)=r;
    i=i+1;
end
function F = axialV(x,B,rin,rout)
F = [-1*rin^2 + x(1)*log(rin) - B*rin + x(2) ;
    -1*x(5)^2 + x(1)*log(x(5)) - B*x(5) + x(2) - x(7) ;
    -2*x(5) + x(1)/x(5) - B ;
    -1*x(6)^2 + x(3)*log(x(6)) + B*x(6) + x(4) - x(7) ;
```

```
-1*rout^2 + x(3)*log(rout) + B*rout + x(4);
-2*x(6) + x(3)/x(6) + B ;
x(6) - x(5) - B];
```

```
function [W,DW,DDW,r,r1,r2,ap]=Daxial2_up(B,eta,N)
% The characteristic length is d=R2-R1
%eta=R1/R2;
%Bingham Number
c=axial2(eta,B); %Calculating the constants for
%axial velocity
% Calculating chebychev points and transforming to
% cylindrical coordinate
%N number of chebycheve nodes
R1=eta/(1-eta);
R2=1/(1-eta);
j=(0:1:N)';
y=cos(j*pi/N);
%velocity profile
r1=c(5);%Inner plug radius
r2=c(6);%Outer plug radius
ap=(r2-r1);
if B==0
    r=(R2-R1)/(2)*y+(R2+R1)/(2);
    for i=1:N+1
        if r(i) < r1
            W(i)=-1*r(i)^2+c(1)*log(r(i))-B*r(i)+c(2);
            DW(i)=-2*r(i)+c(1)/r(i)-B;
            DDW(i)=-2-c(1)/r(i)^2;
        end
        if r(i) > r1 && r(i) < r2
            W(i)=c(7);
            DW(i)=0;
            DDW(i)=0;
        end
        if r(i) > r2
            W(i)=-1*r(i)^2+c(3)*log(r(i))+B*r(i)+c(4);
            DW(i)=-2*r(i)+c(3)/r(i)+B;
            DDW(i)=-2-c(3)/r(i)^2;
        end
    end
else
    r=(R2-r2)/(2)*y+(r2+R2)/(2);
```

```
    for i=1:N+1
        W(i)=-1*r(i)^2+c(3)*log(r(i))+B*r(i)+c(4);
        DW(i)=-2*r(i)+c(3)/r(i)+B;
        DDW(i)=-2-c(3)/r(i)^2;
    end
end
W=W'*ones(1,N+1);
DW=DW'*ones(1,N+1);
DDW=DDW'*ones(1,N+1);
```

```
function [D0,D1,D2,D3,D4]=ChebyshevPolynomial(N)
%Creating Tn(y)
%The matrix D0
(zero derivative) is arrange as the first
%column represents T0(y), the second T1(y) and so on.
% N=5;
D0=zeros(N+1,N+1);
j=(0:1:N)';
y=cos(j*pi/N);
D0(:,1)=1;
D0(:,2)=y;
for n=2:N
    D0(:,n+1)=2*y.*D0(:,n)-D0(:,n-1);
end

%Creating T'n(y)
D1=zeros(N+1,N+1);
D2=zeros(N+1,N+1);
D3=zeros(N+1,N+1);
D4=zeros(N+1,N+1);
%
D1(:,1)=0;
D1(:,2)=D0(:,1);
for n=3:N+1
    D1(:,n)=2*D0(:,n-1)+2*y.*D1(:,n-1)-D1(:,n-2);
    D2(:,n)=4*D1(:,n-1)+2*y.*D2(:,n-1)-D2(:,n-2);
    D3(:,n)=6*D2(:,n-1)+2*y.*D3(:,n-1)-D3(:,n-2);
    D4(:,n)=8*D3(:,n-1)+2*y.*D4(:,n-1)-D4(:,n-2);
end
```

```
function [Vi, E] =
 evaluesian2(Re1,k,B,eta,N,W,DW,DDW,r,V,DV,r2)
% Input:
% Re1   Axial Re number
% k=alpha   wavenumber, k >= 0
% B is the Bingham number
% eta=R1/R2 < 1 is the radius ratio
% N is the number of Cheby polynomials
% All SCALARS
% Output:
% E     VECTOR of eigenvalues of the system
% V  coefficients of eigenvectors in Cheby expansion
% Method: Call Matlab's eig function
alpha=k;
warning off MATLAB:divideByZero
% internal stuff
num =round(abs(N));
nosmod=N;

if B==0
 R1=eta/(1-eta);% Inner and outer radious in meter.
else
    R1=r2;
end
R2=1/(1-eta);
scale = 2/(R2 - R1);
[D0,D1,D2,D3,D4]=ChebyshevPolynomial(N);
er = -200000;
Nos = nosmod + 1;
% velocity profile etc
for i = 1:num+1
    rinv1(i) = 1/r(i);
    rinv2(i) = 1/r(i)^2;
    rinv3(i) = 1/r(i)^3;
    rinv4(i) = 1/r(i)^4;
end;
rinv1 = rinv1'*ones(1,N+1);
rinv2 = rinv2'*ones(1,N+1);
```

```
rinv3 = rinv3'*ones(1,N+1);
rinv4 = rinv4'*ones(1,N+1);
%===================================
%   Ax = \lambda Bx
%===================================
%   Radial momentum equation
%================================
D1=D1*scale;
D2=D2*scale^2;
D3=D3*scale^3;
D4=D4*scale^4;
Phi_tetha=-alpha^2./abs(DW).*D0+2*(D1-D0.*rinv1)./...
abs(DW).*rinv1+...
    (D2-D1.*rinv1+D0.*rinv2)./abs(DW)-(D1-D0.*rinv1)...
    .*DDW./DW.^2*sign(DW);

Phi_r=2*alpha^2*(2*(D2+D1.*rinv1-D0.*rinv2)./abs(DW)...
    -2*(D1+D0.*rinv1).*DDW./(DW).^2*...
    sign(DW)+D0.*rinv1.*DDW./DW.^2*sign(DW));
A11 = zeros(Nos,Nos);
A11=A11-(D4+2*D3.*rinv1-3*D2.*rinv2+3*D1.*rinv3-3*D0*rinv4);
A11=A11+2*alpha^2*(-D0.*rinv2+D1.*rinv1+D2)-alpha^4*D0;
A11Re=-alpha^3*1i.*W.*D0-alpha*1i*DDW.*D0;
A11Re=A11Re+W.*(D2+D1.*rinv1-D0.*rinv2)*alpha*1i+...
alpha*1i*DW.*D0.*rinv1;
A11=A11+Re1*A11Re+B*Phi_r;

A12=2*Re1*alpha^2*V.*rinv1.*D0;
A21=-Re1*(DV+V.*rinv1).*D0;
A22=(D2+D1.*rinv1-D0.*rinv2-alpha^2*D0)
-1i*alpha*Re1*W.*D0+...
B*Phi_tetha;
A=[A11 A12; A21 A22];
B11=-(D2+D1.*rinv1-D0.*rinv2-alpha^2*D0);
B12=zeros(N+1,N+1);
B21=zeros(N+1,N+1);
B22=D0;
B=[B11 B12;B21 B22];
```

```
%BOUNDARY CONDITIONS
A(1,:)=[er*D0(1,:) zeros(1,N+1)];
A(2,:)=[er*D1(1,:) zeros(1,N+1)];
A(N,:)=[er*D1(N+1,:) zeros(1,N+1)];
A(N+1,:)=[er*D0(N+1,:) zeros(1,N+1)];

A(N+2,:)=[zeros(1,N+1) er*D0(1,:)];
A(N+3,:)=[zeros(1,N+1) er*D1(1,:)];
A(2*N+1,:)=[zeros(1,N+1) er*D1(N+1,:)];
A(2*(N+1),:)=[zeros(1,N+1) er*D0(N+1,:)];

B(1,:)=[D0(1,:) zeros(1,N+1)];
B(2,:)=[D1(1,:) zeros(1,N+1)];
B(N,:)=[D1(N+1,:) zeros(1,N+1)];
B(N+1,:)=[D0(N+1,:) zeros(1,N+1)];

B(N+2,:)=[zeros(1,N+1) D0(1,:)];
B(N+3,:)=[zeros(1,N+1) D1(1,:)];
B(2*N+1,:)=[zeros(1,N+1) D1(N+1,:)];
B(2*(N+1),:)=[zeros(1,N+1) D0(N+1,:)];

%     ----------------------------------
[Vi,E]=eig(A,B);
E=diag(E);
```

```
function [k_crit, eig_max] =
 find_max_eig(Re1,Re2,k_lower,k_upper,B,eta,N)

% Input:
% Re1       inner cylinder Reynolds number, Re1 > 0
% Re2       outer cylinder Reynolds number
% k_lower   lower bound on wavenumber k
% k_upper upper bound on wavenumber k, k_upper > k_lower
% B is the Bingham number
% eta < 1 is the radius ratio
% N is the number of Cheby polynomials
% All SCALARS
%
% Output:
% eig_max   - real scalar
%       - max real value in the vector of eigenvalues
%           for the system at (Re1, Re2).
%         - Eigenvalues are a function of k.
%
% Method: Golden Section Search
%(see Introduction to Scientific Computing)
    smallnum = 0.0002;
    K_up = k_upper;
    K_low = k_lower;
    [W,DW,DDW,r,r1,r2,ap]=Daxial2_up(B,eta,N);
    [V,DV]=Vvelocity(B,eta,N,Re1,Re2,r2);
ratio = (3-sqrt(5))/2;
c = k_lower + ratio*(k_upper - k_lower);
d = k_lower + (1-ratio)*(k_upper-k_lower);
%    disp([k_lower, c, d, k_upper])
    [Vi, Eig_zero] =
    evaluesian2(Re1,0,B,eta,N,W,DW,DDW,r,V,DV,r2);
    real_Eig_zero = max(real(Eig_zero));
    [Vi, Eig_c] =
    evaluesian2(Re1,c,B,eta,N,W,DW,DDW,r,V,DV,r2);
    [Vi, Eig_d] =
    evaluesian2(Re1,d,B,eta,N,W,DW,DDW,r,V,DV,r2);
real_Eig_c = max(real(Eig_c));
```

```
    real_Eig_d = max(real(Eig_d));
    tolerance = eps*max(abs(c),abs(d));
while (d-c) > tolerance
if real_Eig_c >= real_Eig_d     % move to the left

 %     disp('eig left >= eig right, move to the left')

           real_Eig_d = real_Eig_c;

           k_upper = d;
           d = c;
           c = k_lower + ratio*(k_upper-k_lower);

 %          disp([k_lower, c, d, k_upper])

          [Vi, Eig_c] =
       evaluesian2(Re1,c,B,eta,N,W,DW,DDW,r,V,DV,r2);
          real_Eig_c = max(real(Eig_c));


else                        % move to the right

           real_Eig_c = real_Eig_d;

 %    disp('eig left < eig right, move to the right')

   k_lower = c;
   c = d;
           d = k_lower + (1-ratio)*(k_upper - k_lower);

 %          disp([k_lower, c, d, k_upper])

           [Vi, Eig_d] =
           evaluesian2(Re1,d,B,eta,N,W,DW,DDW,r,V,DV,r2);
           real_Eig_d = max(real(Eig_d));

end
```

```
     tolerance = eps*max(abs(c),abs(d));
 end

 if abs(K_up - k_upper) < smallnum
[k_crit, eig_max] =
find_max_eig(Re1,K_low, K_up^2,B,eta,N)

 else
 [Vi, Eig_average] =
evaluesian2(Re1,(c+d)/2,B,eta,N,W,DW,DDW,r,V,DV,r2);
     real_Eig_average = max(real(Eig_average));
     if real_Eig_average > real_Eig_zero
         eig_max = real_Eig_average;
         k_crit = (c+d)/2;
     else
         eig_max = real_Eig_zero;
         k_crit = 0;
     end
 end
```

```
function [Re_zero]=Re_lambda(eta,Re1,Re2,N,B)
x0=Re1;
Re_zero = fzero(@myfun,x0,[],Re2,eta,N,B);


function eig_max = myfun(Re1,Re2,eta,N,B)
% Re1=2*10^7;
k_lower=0;
k_upper=10;
% eta=0.2;
% N=25;
[k_crit, eig_max] =
find_max_eig(Re1,Re2,k_lower,k_upper,B,eta,N);
```

```
 function [V,DV]=Vvelocity(B,eta,N,Re1,Re2,r2)
% eta=0.9;
% N=50;
% Re1=100;
% Re2=0;
 R2=1/(1-eta);
 omega=Re2/(Re1*R2);
if B==0
    R1=eta/(1-eta);
else
    R1=r2;
end
R1=eta/(1-eta);
j=(0:1:N)';
y=cos(j*pi/N);
r=(R2-R1)/(2)*y+(R2+R1)/(2);
V=r.*omega;
DV=omega;
V=V*ones(1,N+1);
DV=DV*ones(N+1,N+1);
```